Diamond under extreme strains

Candidate: Alaa Mohammed Idris Bakhit (abakhit@eaifr.org)

Supervised by: Prof. Sandro Scandolo

ICTP-East African Institute for Fundamental Research (EAIFR)
University of Rwanda

14 October 2020

Thesis submitted for the full fulfilment of Masters Degree at EAIFR, University of Rwanda

Similarity Index 19%

1 Abstract

In this thesis, we performed ab-initio calculations of the vibrational frequencies of diamond along the crystal direction [001]. We observed the pressure dependence on the Raman shift of diamond. Due to the non-hydrostatic stress, we observed splitting of the triply degenerate first-order Raman mode into doublet ω_D and singlet ω_S. Furthermore, the theory was found to be inconsistent with the observed splitting of the first-order Raman mode. The radial σ_r and axial σ_z stress components were varied at different constant volumes. We obtained a simple polynomial approximation for the dependence of ω_D and ω_S on σ_r and σ_z. In addition, for experimentally measured vibrational frequencies the shear stress ($\tau = \sigma_z - \sigma_r$) was computed. The shear stress points out the non-hydrostatic contribution to the measured sample pressures. Thus, the stress state was obtained for pressures between 200 and 400 GPa which shows the stress state of the diamond anvil cell at multimegabar pressures.

Acknowledgement

First of all I take this golden opportunity to thank Allah for His mercy upon my life. His holy name will always be praised for His good deeds to my success.

I wish to express heartfelt appreciation and thank to the Organization for Women in Science for the Developing World (OWSD), for giving me this opportunity to pursue my Master's degree at ICTP-EAIFR, University of Rwanda.

I sincerely thank my supervisor, Prof. Sandro Scandolo, for his kind help, encouragement, inspiration and support to ensure that this thesis is of good quality. Without him this work could not have been successful. I pass my appreciation more to the supportive Academic Director Dr. Omololu Akin-Ojo for encouragement, inspiration and for his help through the master programme and during my thesis period. I also thank my friend Moritz Fischer for his help.

Last but not least, I thank my mother Fatima Mohammed Awad and my late father Mohammed Idris Bakhit for their great support towards ensuring I acquire knowledge that is useful in my life.

Contents

2 Introduction

High-pressure studies, as well as high-temperature ones, are crucial for experimental exploration of our planet and other planets interior because of the extreme conditions deep inside planets, as shown in Figure 2.1. These extreme conditions could be achieved in the lab, to study the behaviour of matter, a deeper understanding of matter and synthesize new materials. Since geoscientists are not able to access the earth's interior and other planets, in a direct way.

Thus, the Diamond Anvil Cell (DAC) is the most common ways of creating such extreme conditions. A tiny sample of material is confined between two diamonds as shown in Figure 2.2. Diamonds are used because of their hardness and incompressibility, so the pressure generated can be enormous in a very small area: up to a million times of the atmospheric pressure. Scientists can reveal the sample crystal structure and observe them with numerous forms of electromagnetic waves e.g. visible light. By studying how the materials change under high pressure and temperature in DAC, opens new horizons to better understand and model how the same material behaves in the deep interior of the earth and other planets such as extraterrestrial planets. For example, recent discoveries were made in the field of high pressure condensed matter physics which include the metallization of hydrogen as high-temperature superconductor found by Dias and Silvera at 495 GPa in their experiments [1] [2], as well as developing microelectronics from new forms of Silicon and more powerful batteries made up using new materials [3] and nano-tubes used to produce an extremely strong building materials [4]. Dubrovinskaia et. al. [5] were able to synthesize an optically transparent micro-balls of bulk nano-crystalline diamond.

To study materials properties under high static pressure the Diamond Anvil Cell (DAC) device is used, shown in Figure 2.2. DAC contains a pair of opposite anvils made of diamond and a metal gasket made of a highly incompressible material. Tungsten, Kapton and Rhenium are commonly used. The gasket is used to keep the sample when the pressure is applied to it. DAC design was established in the 20^{th} century by **Percy W. Bridgman** Nobel laureate winner in 1946 for his high pressure studies [9]. Recently, the standard DACs have reached high pressures up to 425 GPa at room temperature, and 1 TPa with designs [5].

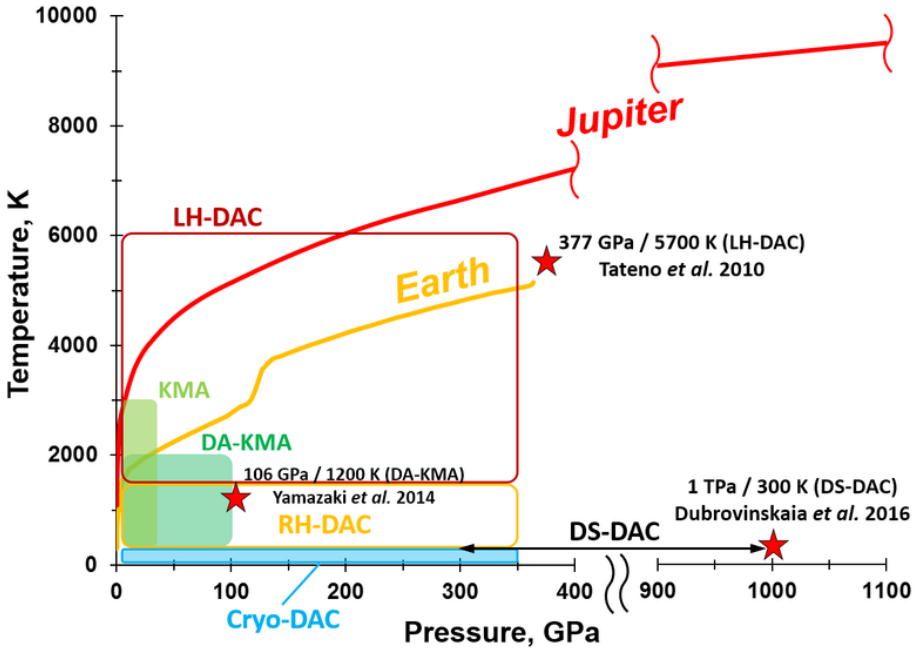

Figure 2.1: Conditions achievable using different methods of static pressure generation: LH-DAC stands for diamond anvil cell with laser heating [6]; RH-DAC is diamond anvil cell with resistive heating [7]; DS-DAC stands for double-stage diamond anvil cell [5]; KMA - Kawai multi-anvil apparatus; DA-KMA stands for diamond-anvil Kawai multi-anvil apparatus. Earth geotherm and a part of Jupiter geotherm are shown for comparison [8].

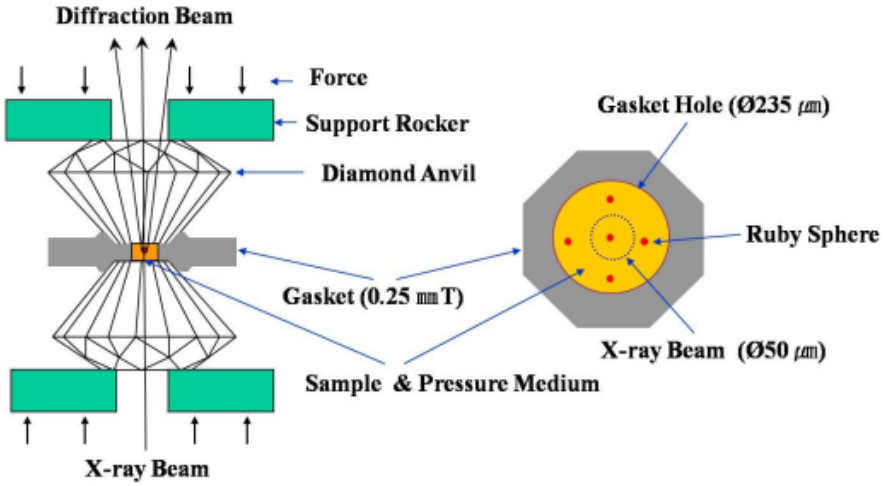

Figure 2.2: Schematic diagram of the Diamond Anvil Cell (DAC) [10].

2.1 Objectives

Despite the simplicity of the DAC design, determining the pressure on the sample still poses a challenging task. There are several methods to determine the pressure on the

sample such as x-ray diffraction, ruby fluorescence method and the recently used Raman spectroscopy method. In this thesis, we will consider the Raman spectroscopy method as a universal pressure calibration method that could push further the research on the determination of the sample pressure in the DAC experiments. The Raman method is based on the observed dependence of the high-frequency edge of the diamond Raman absorption spectrum in a DAC, on the pressure in the sample. The main goal of this thesis is to shed light on this relation by means of ab-intio calculations of the Raman frequency of diamond under arbitrary strain conditions. Furthermore, an important objective is to broaden our understanding of the stress-strain state in a DAC.
Our principal objectives are as follows:

1. Determining with first-principle methods the vibrational frequencies of diamond at strain conditions typical of Diamond Anvil Cells (DAC).

2. Theoretical data will be compared with experimental data and used to re-calibrate the pressure scale used in experiments.

3. Understanding the stress-strain state of the diamond anvil.

2.2 Outlines

In chapter 2, we give an introduction to high pressure studies and recent discoveries. Also, we introduce DAC.
In chapter 3, we will introduce the pressure determination methods and discuss the diamond structure.
In chapter 4, we will explore the theoretical background of density functional theory used in calculations. In addition, we will show convergence tests and obtain optimal parameters.
In chapter 5, we will show the procedure of calculating vibrational frequencies, using the optimized parameters. Besides, we will discuss the obtained results.
In chapter 6, we will summarise the present work, draw conclusions and outline possible future directions.

3 Literature Review

3.1 Diamond

Diamond has unique properties which are, its extraordinary hardness and a wide range of optical transmission as well as high thermal conductivity as a result of possessing a strong bonding [11]. Accordingly, it has become an ideal candidate for many scientific investigations in high-pressure physics. These characteristics are exploited heavily in mechanical and technical applications. Also, it is known for pressure resistivity, therefore, a perfect candidate to construct the Diamond Anvil Cell (DAC) devices involved in high pressures studies generating up to multimegabar pressures.

In Diamond crystal, Carbon atoms are arranged such that its structure consists of two inter-penetrating face centred cubic Bravais lattices, with two Carbon atoms located at $(0, 0, 0)$ and $(\frac{1}{4}, \frac{1}{4}, \frac{1}{4})$ in crystal units along the body diagonal of the cube in a primitive basis unit cell as shown in Figure 3.1. It is also the crystal structure of the semiconductors silicon and germanium [12].

Diamond is considered as the hardest of all known solids. Thus, it is used in the DAC, which is capable of creating a static pressures exceeding 1 TPa [5]. One of the tremendous advantages of using diamond anvils is that they are transparent to many forms of radiation from x-ray to visible and infrared radiation. It enables to explores a wide range of experimental probes.

Under extreme pressure, the diamond crystal experiences deformations of the culet face, the face facing the sample, as shown in Figure 3.1. Under compression along one of the cubic axes, diamond structure loses its cubic symmetry and has to be described as a body-centred tetragonal (bct) containing two atoms [13], further details are given in chapter 4. This has been observed with x-ray diffraction. This observations led to finite-element calculations of diamond deformations [14] to explore the geometric properties of a diamond anvil, as well as first-principle calculations of the stress-strain curve of diamond [13]. At extreme conditions typical to DAC a theoretical upper bound to the ultimate yield strength was obtained of diamond from first principles calculations. Diamond is mechanically stable against tetragonal shear instabilities for $\sigma_z - \sigma_r < 200$ GPa, where σ_z is the axial and σ_r is the radial components of the stress tensor [13].

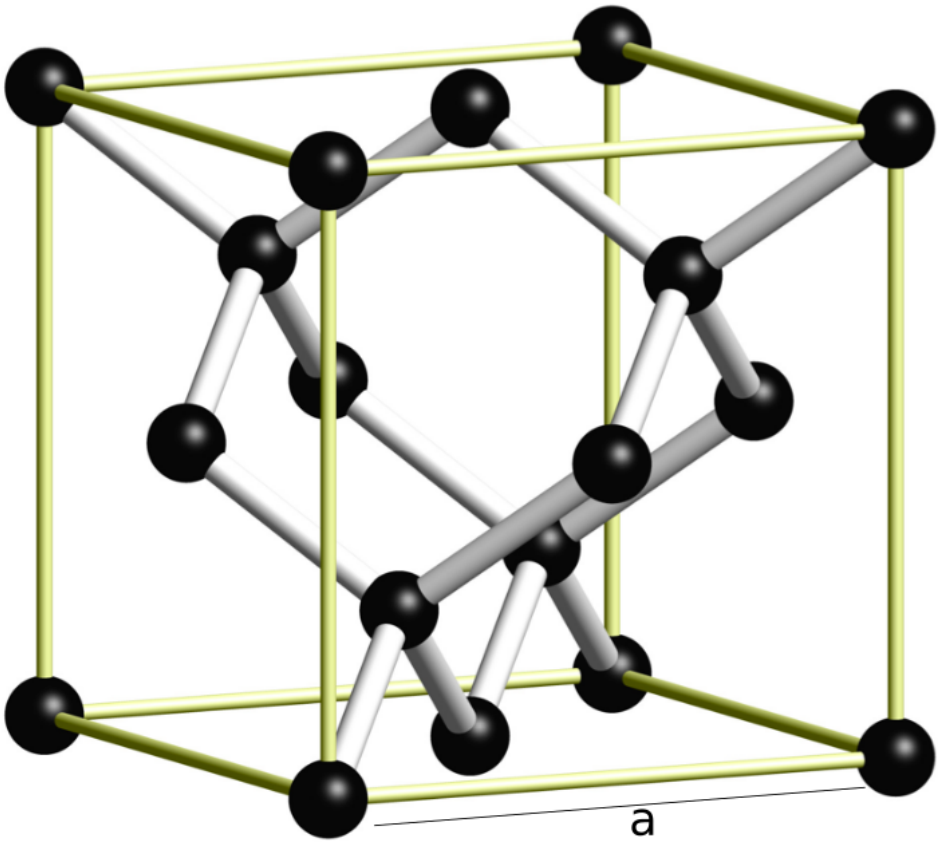

Figure 3.1: The diamond structure is shown, the lattice parameter, **a**, for Diamond, it is 3.57 **Å** [12] [15].

3.2 Pressure Determinations Methods

A very commonly used method in pressure determination is **the Ruby fluorescence method** as a pressure gauge in DAC experiments [16]. Using a focused laser to illuminate a tiny ruby, the ruby it will glow in distinctive fluorescence lines at ambient pressure. The ruby fluorescence lines under pressure experience a shift which depends on the applied pressure. A disadvantage of the ruby is when it is heated the fluorescence peaks broaden, this leads to a weakening of the fluorescence signal so their positions can no longer be measured. Moreover the non-hydrostatic pressure effects make the method inapplicable for pressures higher than $100-150$ GPa [17]. Another method to determine the pressure in the sample is using an equation of state (EOS) of standard materials. For example, Pt, Au, Ag have been used for pressures >150 GPa as a gasket, pressure determination method, x-ray diffraction to measure the lattice spacing of a material for which the EOS is known to obtain the volume [17]. The use of EOS technique requires access to an x-ray source which considered to be a disadvantage of the method.

Subsequently to the failure of ruby fluorescence method at pressures >150 GPa, a new optical method was proposed by **Hanfland and Syassen** [18]. The first-order Raman mode of diamond is used commonly as a pressure gauge and it is the only appropriate method in very high-pressure determination. It is based on the monotonic dependence of the Raman shift on pressure. This thesis will foocus on the Raman spectroscopy method.

3.3 The Raman Spectroscopy Method

In Raman spectroscopy, the laser beam is aligned parallel to the principal axis of the diamond anvil. Before the beam reaches the sample chamber it traverses completely the diamond anvils from virtually unstrained state near to the loading face up to the state with the highest strain near to the culet face of the diamond anvil. This gives raise to a band extended from the intense first order Raman peak at 1332 cm^{-1} [11] at ambient pressure to the highest frequency resulting from the maximum strain close to the culet face. The Raman band is produced by the scattering of the Raman signal from the continuum of diamond strain states probed by the beam.

In the absence of stress (ambient conditions), optical phonons of the diamond are triply degenerated and the Raman spectra with Raman line at 1333 ± 1 cm^{-1} [17], as shown in Figure 3.2. Upon the application of stress the triply degenerate Raman

spectra shift or/and split into two low-high frequency refereed to the unstressed table face and the stressed culet face of the diamond anvil, respectively [19]. **Hanfland and Syassen** [18] were the first to calibrate diamond as a pressure gauge.

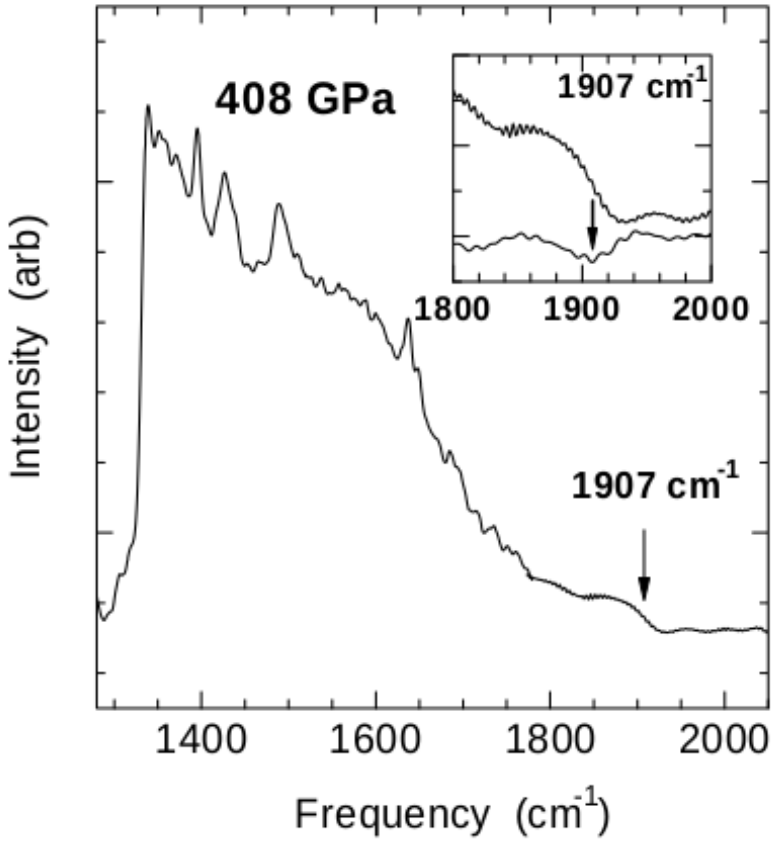

Figure 3.2: Typical Raman spectra from the center of the diamond anvil culet at 408 GPa [19].

Several studies are conducted to obtain a universal curve that describes the relationship between the first-order Raman frequency of the culet centre of the diamond anvil and the pressure e.g. [20] [14][17] and [19] in Raman spectroscopy method. New pressure calibrations are necessary in different diamond anvil cell configurations. The specific shape of a diamond edge depends on the configuration of the optical setup and the pressure conditions used. Since the strain states of the diamond in a DAC are not known, the specific dependence of the high-frequency Raman edge on the sample pressure. Providing accurate constraint is the main goal of this thesis.

4 Methodology

4.1 Introduction

In this chapter, we will explore the biggest challenge of understanding properties of materials used in our daily life. This relies upon understanding the behaviour of their electrons this implies understanding their electronic structure and the dynamic of their nuclei [21]. Our discussion will be in qualitative aspects about the many-body Hamiltonian, the Born-Oppenheimer approximation and Density Functional Theory (DFT).

4.2 The Electronic Problem

4.2.1 Many Body Hamiltonian

The description of the system starts with the many-body non-relativistic Hamiltonian [22] given by

$$\hat{H} = T_e + T_n + V_{ee} + V_{en} + V_{nn}, \tag{4.2.1}$$

where,

$T_e = -\sum_{i=1}^{N_e} \frac{\hbar^2}{2m_i} \vec{\nabla}_i^{\,2}$ is the kinetic energy of electrons,

$T_n = -\sum_{I=1}^{N_n} \frac{\hbar^2}{2m_I} \vec{\nabla}_I^{\,2}$ is the kinetic energy of nuclei,

$V_{ee} = \frac{1}{2} \sum_{i \neq j} \frac{e^2}{|\vec{r_i} - \vec{r_j}|}$ is the Coulomb repulsion between electrons,

$V_{nn} = \frac{1}{2} \sum_{I \neq J} \frac{Z_I Z_J e^2}{|\vec{r_I} - \vec{r_J}|}$ is the Coulomb repulsion between nuclei, and

$V_{en} = -\frac{1}{2} \sum_{i \neq I} \frac{Z_I e^2}{|\vec{r_i} - \vec{r_I}|}$ is the Coulomb attraction between electrons and nuclei.

Lower case subscripts denote electron properties and upper case subscripts denote nuclei features M_I and Z_I are masses and atomic number of nucleus I, and $\vec{r}$ represents coordinates.

Indeed, to give a realistic description of a real material one needs to solve the full non-relativistic time independent Schrödinger equation,

$$\hat{H}\Psi_i(\vec{r}, \vec{R}) = E\psi_i(\vec{r}, \vec{R}), \tag{4.2.2}$$

where E is the energy and $\psi_i(\vec{r}, \vec{R})$ is the many-body wave-function.

However, the problem is not an easily solvable one since there are of the order of

10^{23} interacting particles in the solid per cm^3. Approximate methods must be used and simpler models developed for solving the problem.

In order to explore the properties of the system, many approximations are used to at least obtain an estimate of the solution. One of the commonly used ones is the Born-Oppenheimer approximation, discussed below.

4.2.2 The Born Oppenheimer Approximation

This approximation is based on the comparative behaviour of electrons and nuclei. Electrons have masses lighter than nuclei, therefore nuclei move slower [22]. Hence, we can consider the electrons in the system as moving in a field of the fixed nuclei. This will enable us to deal separately with the electronic and nuclear degrees of freedom as follows:

$$\psi(\{\vec{r_i}\};\{\vec{R_I}\}) = \phi(\{\vec{r_i}\};\{\vec{R_I}\}).\chi(\{\vec{R_I}\}), \tag{4.2.3}$$

$$\hat{H}\psi(\{\vec{r_i}\};\{\vec{R_I}\}) = [T_e + T_n + V_{ee} + V_{en} + V_{nn}]\psi(\{\vec{r_i}\};\{\vec{R_I}\}) = E\psi(\{\vec{r_i}\};\{\vec{R_I}\}), \tag{4.2.4}$$

where ϕ is the wave-function of the electrons at fixed nuclei coordinates and χ is that of the nuclei.
Substituting Expression (4.2.3) into Equation (4.2.4), we obtain the following:

$$\left[-\sum_{I=1}^{N_n}\frac{\hbar^2}{2m_I}\vec{\nabla}_I^2 + \frac{1}{2}\sum_{I\neq J}\frac{Z_I Z_J e^2}{|\vec{r_I}-\vec{r_J}|} + U(\{\vec{R_I}\})\right]\chi(\{\vec{R_I}\}) = E_n\chi(\{\vec{R_I}\}). \tag{4.2.5}$$

Equation (4.2.5) is the nuclear Schrödinger equation, which describes the motion of the nuclei in the average field of the electrons [22]. The function $U(\{\vec{R_I}\})$ is given by:

$$U(\{\vec{R}\}) = \int d^{3N}\vec{r_i}\phi^\star\left[-\sum_{i=1}^{N_e}\frac{\hbar^2}{2m_i}\vec{\nabla}_i^2 + \frac{1}{2}\sum_{i\neq j}\frac{e^2}{|\vec{r_i}-\vec{r_j}|} - \frac{1}{2}\sum_{i,I}\frac{Z_I e^2}{|\vec{r_i}-\vec{R_I}|}\right]\phi, \tag{4.2.6}$$

and ϕ satisfies:

$$\left[-\sum_{i=1}^{N_e}\frac{\hbar^2}{2m_i}\vec{\nabla}_i^2+\frac{1}{2}\sum_{i\neq j}\frac{e^2}{|\vec{r_i}-\vec{r_j}|}-\frac{1}{2}\sum_{i,I}\frac{Z_I e^2}{|\vec{r_i}-\vec{R}_I|}\right]\phi(\{\vec{r_i}\},\{\vec{R}_I\})=E_e\phi(\{\vec{r_i}\},\{\vec{R}_I\}). \tag{4.2.7}$$

Equation (4.2.7) represents the electronic Schrödinger equation. The electronic structure problem focuses solely on Equation (4.2.7) and tries to find a solution for given nuclei positions using only the electronic Hamiltonian and the electronic wave function [22]. Equation (4.2.6) introduces the concept of potential energy surfaces where the nuclei move and it is obtained first by solving the electronic problem. Thus the nuclei move on a potential energy surface found by solving the electronic problem.

In summary the Born-Oppenheimer approximation is about separating the electronic and nuclear degrees of freedom. It is a good approximation in the case where there is a large electronic energy gap between the ground state and the excited states of the electrons Hamiltonian.

4.2.3 Hatree-Fock Approximation

As mentioned previously, the electronic Hamiltonian depends only on the spatial coordinates of electrons, these of the nuclei are fixed. As electrons are spin $\frac{1}{2}$ fermions, we need to specify their spin. We describe their spins by the coordinate s and we let $x \equiv (\vec{r}, s)$ represent the full spin-position coordinates. Since electrons are indistinguishable. Fermions, not only must the wavefunction ϕ satisfy the Schrödinger equation the wave function of the many electron system has to be antisymmetric regarding the interchange of coordinates.

$$\phi(x_1, x_2, ..., x_N) = -\phi(x_2, x_1, ..., x_N), \tag{4.2.8}$$

this corresponds to the well known Pauli exclusion principle, which says that a spin-orbital can be occupied by at most one electron [22].

In the case of non-interacting fermions, this condition can be written as a properly antisymmetrized linear combination of one-electron functions corresponding to a (Slater) determinant. In particular,

$$\phi(x_1, x_2, ..., x_N) = \frac{1}{\sqrt{N!}} \begin{vmatrix} \psi_i(x_1) & \psi_j(x_1) & \cdots \\ \psi_i(x_2) & \psi_j(x_2) & \cdots \\ \vdots & \cdots & \ddots \end{vmatrix}, \tag{4.2.9}$$

where $\psi_i, \psi_j, \cdots$ represent the N lowest one-electron states of the system of N electron and $x_1, \cdots, x_N$ are the coordinates (spin and positions) of the electrons.

For interacting electrons a single Slater determinant is not sufficient and are has to use a linear combination of such determinant,

$$\psi(x_1, \cdots, x_N) = \sum_n a_n \phi(x_1, \cdots, x_N), \tag{4.2.10}$$

where $\phi(x_1, \cdots, x_N)$ are different (excited) Slater determinants typically obtained from Expression (4.2.9) by replacing one or more single orbital ψ_j with energies higher then those of the N lowest ones.

Expression (4.2.10) leads to complicated equations because many determinants are involved. Thus, one tries to find the best single determinant in a variational approach to solving the electronic problem. This leads to the Hatree Fock (HF) approximation

In the **Hatree Fock (HF) approximation,** the many electron wave function is expressed by a single Slater determinant $|\psi> \simeq |\phi>$. This determinant can be found by determining the optimal spin orbitals ψ_j, that minimize the energy $E = \frac{<\phi|\hat{H}|\phi>}{<\phi|\phi>}$ where,

$$\hat{H}_e = -\sum_{i=1}^{N_e} \frac{\hbar^2}{2m_i} \vec{\nabla}_i^2 + \frac{1}{2} \sum_{i \neq j} \frac{e^2}{|\vec{r_i} - \vec{r_j}|} - \frac{1}{2} \sum_{i,I} \frac{Z_I e^2}{|\vec{r_i} - \vec{R}_I|}. \tag{4.2.11}$$

The optimal ϕ obtained describes the HF ground state of an N electron system [22]. The essence of the HF approximation is to replace the complexity of solving N electron system by one-electron problems in which the electron repulsion is treated in an average way. The difference between the formal electron energy E_0 and the HF energy E_{HF} is called the correlation energy $E_{corr} = E_0 - E_{HF}$. The HF potential or equivalently, the field which is seen by the i^{th} electron depends on spin orbitals of the other average j^{th} electrons. Thus, the HF equation is non-linear and must be solved iteratively. The procedure for solving the HF equation is called the self-consistent field SCF method [22].

The HF method works well in the case where the so-called electron correlation energy is small. If this correlation energy is significant, are must resat to other methods that include the correlation energy. Next, we introduce **Density Functional Theory**

(DFT), which is the most widely used method for attempting to capture the correlation energy.

4.3 Density Functional Theory

While density functional theory (DFT) attempts to recover the correlation energy E_{corr}, it is a different approach to solving the electronic problem. It is not based on a many electrons wave function. but on the scalar quantity, the electron density, which can be found easily at any point in space. Moreover, the particle number is determined by the density. DFT is the most widely used theory for electronic systems investigations [23]. It is exact in principle, the ground state energy is a central quantity in DFT and it can be calculated accurately in principle and efficiently as a functional of the density. Thus the ground-state electron density determines the Hamiltonian operator and subsequently all properties of the electronic system. The Hohenberg-Kohn theorem and Kohn Sham equations are the bass of the present day popular DFT formulations. A detailed description of these are given below.

4.3.1 The Hohenberg-Kohn Theorem

In 1964, Density Functional Theory (DFT) was formally established by Hohenberg and Kohn [24]. They used reductio ad absurdum (proof by contradiction) to prove the uniqueness of the density considering the case of a non-degenerate ground state in their derivation [24]. As mentioned in the following;

Theorem 1: The potential is a unique functional of the electron density n($\vec{r}$), for an arbitrary number of electrons in a box subjected to an external potential $V_{ext}(\vec{r})$ and the electron-electron Coulomb repulsion, except for an additive constant [24].

Theorem 2: The sum of the kinetic and electron-electron interaction energies is a universal functional of the charge density, since ψ is a functional of n($\vec{r}$) [24].

The energy functional of n($\vec{r}$) for a given potential $V_{ext}(\vec{r})$ will be

$$\begin{aligned} E[n(\vec{r})] &= T[n(\vec{r})] + E_{int}[n(\vec{r})] + \int V_{ext}(\vec{r})n(\vec{r})d\vec{r} + E_{nn} \\ &\equiv F[n(\vec{r})] + \int V_{ext}(\vec{r})n(\vec{r})d\vec{r} + E_{nn}. \end{aligned} \tag{4.3.1}$$

where $F \equiv T + E_{int}$ Furthermore, Hohenberg and Kohn proceeded to determine the minimum of the unique functional $E[n(\vec{r})]$ of the exact ground state density n($\vec{r}$) given

that the total number of particles N is constant,

$$N[n(\vec{r})] \equiv \int n(\vec{r})d\vec{r} = N. \tag{4.3.2}$$

They have shown that the density $n^{'}(\vec{r})$, associated with another potential $V_{ext}^{'}$ led to a minimum value of the energy higher than the one determined previously $E[n(\vec{r})]$ with the ground state density n($\vec{r}$) of the system [24]. So, the following inequalities were established:

$$\int V_{ext}(\vec{r})n^{'}(\vec{r})d\vec{r} + F[n^{'}] > \int V_{ext}(\vec{r})n(\vec{r})d\vec{r} + F[n]. \tag{4.3.3}$$

It worth pointing out that the potential $V_{ext}(\vec{r})$ is used on both sides of the inequality. The results obtained from Equation (4.3.3) are known as the second Hohenberg and Kohn theorem or as the DFT **variational principle** [24]. These theorems, however, do not give any idea about the energy functional $F[n(\vec{r})]$ nor how to construct it. In fact, this functional is unknown and only approximations exit. The functional $F[n(\vec{r})]$ contains two parts: the unknown kinetic energy density function $T[n(\vec{r})]$ and the equally unknown functional $E_{int}[n(\vec{r})]$ describing the electron-electron interaction energy.

4.3.2 The Kohn-Sham Formalism

Kohn and Sham (1965) attempted to obtain an approximation to $F[n(\vec{r})]$. They suggested a model system of hypothetical non-interacting electrons instead of the many-electrons problem. The Kohn-Sham (K-S) wave function is defined as an eigenstate of a hypothetical non-interacting electron system [23] and determines properties of the real system, in particular the ground-state energy. The energy functional proposed by K-S can be written as,

$$E[n(\vec{r})] = T[n(\vec{r})] + E_H[n] + E_{ext}[n(\vec{r})] + E_{xc}[n(\vec{r})]. \tag{4.3.4}$$

The terms in Expression (4.3.4) above are:

$T[n(\vec{r})] = \sum_{i=1}^{N_e} \langle\phi_i|\frac{\hbar}{2m}\vec{\nabla}^2|\phi_i\rangle$ is the kinetic energy of a system of non-interacting electrons with density n($\vec{r}$), this term is written in terms of assumed hypothetical orbitals, called the K-S orbitals. These orbitals are related to the ground state density n($\vec{r}$) by n($\vec{r}$)=$\sum_i |\phi_i|^2$ and both sums are over only the occupied orbitals.

$E_H[n] = \frac{1}{2}\int\int d\vec{r_1}d\vec{r_2}\frac{n(\vec{r_1})n(\vec{r_2})}{|\vec{r_1}-\vec{r_2}|}$ is Hatree energy,

$E_{ext}[n(\vec{r})] = \int d\vec{r} V_{ext}(\vec{r}) n(\vec{r})$ is energy due to the external potential $V_{ext}(\vec{r})$,

$E_{xc}[n(\vec{r})]$ is the exchange correlation energy of a system of interacting electrons with the same density n($\vec{r}$).
Minimizing the expression in (4.3.4) above with respect to n($\vec{r}$) subject to the constraint that the orbitals ϕ_i are orthonormal leads to the Kohn and Sham self-consistent equations are given as:

$$\left[-\frac{\hbar^2}{2m}\vec{\nabla}^2 + V_{eff}\right]\phi_i(\vec{r}) = E_i\phi_i(r), \tag{4.3.5}$$

$$V_{eff}(\vec{r}) = V_{ext}(\vec{r}) + \frac{\delta E_H[n(\vec{r})]}{\delta n(\vec{r})} + \frac{\delta E[n(\vec{r})]}{\delta n(\vec{r})}. \tag{4.3.6}$$

assumed hypothetical orbitals called **Kohn Sham orbitals**

Kohn and Sham also obtained an expression for $E_{xc}[n]$ in terms of the exchange-correlation energy per electron of a homogeneous gas whose density is constant and the same everywhere in space $n(\vec{r}) = n$. Other approximations exit exchange for the correlation energy functional such as "LDA" and "GGA" which are discussed in the next section.

4.4 Exchange-Correlation Functionals in DFT

There is a tremendous number of exchange-correlation functionals in DFT which can be classified as follows:

4.4.1 Local Density Approximation (LDA)

Local density approximation (LDA) was suggested by Kohn and Sham.

$$E_{xc}[n(\vec{r})] \simeq \int d^3r n(\vec{r}) \varepsilon_{xc}(n(\vec{r})), \tag{4.4.1}$$

where $n(\vec{r})$ is the local density and $\varepsilon_{xc}(n(\vec{r}))$ the exchange-correlation energy per particle of a homogeneous electron-gas having a density n($\vec{r}$).

This approximation is a good one only when considering a homogeneous gas where the density is the same everywhere. But in the case of non-homogeneity, the value of the density varies with space. Consequently, the approximation becomes inaccurate. As we will see later, the LDA is the approximation chosen in this study. A step forward to improve on this by accounting for fluctuations is described next.

4.4.2 Generalized Gradient Approximation (GGA)

In order to improve upon LDA, further corrections are required when considering non-uniform charge densities. A functional of the magnitude of the gradient of the density ∇n as well as the value of n at each point $\vec{r}$ have been proposed;

$$E_{xc}[n(\vec{r})] \simeq \int d^3r n(\vec{r}) \varepsilon_{xc}(n(\vec{r}), |\vec{\nabla} n(\vec{r})|), \tag{4.4.2}$$

where $n(\vec{r})$ is the local density and $\varepsilon_{xc}(n(\vec{r}), |\vec{\nabla} n(\vec{r})|)$ the exchange-correlation energy per particle of homogeneous electron-gas with density n($\vec{r}$); and it also depends on the gradient of the density which gives further information for more accurate results. GGA employs a variety of ways proposed for functions that modify the behaviour at large gradients to preserve desired properties [25].

4.4.3 Meta-GGA

In addition to GGA, the Meta-GGA method relies on a kinetic energy term $\tau(\vec{r}) = \sum_{i=1}^{N} \phi_i^\star(\vec{r}) \vec{\nabla}^2 \phi_i(\vec{r})$:

$$E_{xc}[n(\vec{r})] \simeq \int d^3r n(\vec{r}) \varepsilon_{xc}(n(\vec{r}), |\vec{\nabla} n(\vec{r})|, \tau(\vec{r})), \tag{4.4.3}$$

$\varepsilon_{xc}(n(\vec{r}), |\vec{\nabla} n(\vec{r})|, \tau(\vec{r}))$ is again the exchange-correlation energy per particle of homogeneous electron-gas with the density n($\vec{r}$) but it also depends on $|\vec{\nabla} n(\vec{r})|$ as well as on τ.

4.4.4 Hybrid Functional

The Hybrid Functional is a combination of DFT and HF to avoid the disadvantages of the two methods, given by the following:

$$E_{xc} \simeq E^c_{GGA} + (1-\alpha) E^x_{GGA} + \alpha E^x_{HF}. \tag{4.4.4}$$

Here, the correlation energy is approximated by a GGA E^c_{GGA} while the exchange energy is a linear combination of the GGA correlation energy $E^x_{GGA}[n]$ and the Hatree-Fock like exchange energy E^x_{HF} obtained using K-S orbitals. Precisely,

$$E^x_{HF} = \frac{-e^2}{4} \int d^3r \int \frac{|\gamma(\vec{r}, \vec{r'})|^2}{|\vec{r} - \vec{r'}|} d^3r', \tag{4.4.5}$$

with $\gamma(\vec{r},\vec{r'}) \equiv \sum_i \phi_i^\star(\vec{r})\phi_i(\vec{r'})$, the so-called reduced one-density matrix for non-interacting orbitals.

With E_{xc} defined, one proceed to solve the K-S equations. Typically, the orbitals ϕ_i are expanded using known functions called basis functions. Different basis functions are possible. In this work, plane waves are used as described below.

4.5 Plane Wave Pseudo-potential Method

We discused in subsection 4.2.2 the Born Oppenheimer Approximation which approximately separates the electronic and ionic degrees of freedom, while HF mapped the many electrons wave function into a single Slater determinant and, thus reduces with the complexity of the wave function. DFT, which relies on the density, was proposed as an exact theory to solve the electronic problem. Now, we deal with the question of how to implement these methods and solve the electronic problem together with the simplifications needed to solve the Kohn-Sham self-consistent equations. We will discuss one widely used approach for solids.

4.5.1 Plane Wave Basis Set

More solids in nature have crystaline structure, i.e they are made up of repetition of a basis building block, called the primitive unite cell. Thus, an electron at a point $\vec{r}$ in this solid "feels" the same as that felt by another electron at position $\vec{r}+\vec{R}$, where $\vec{R}$ is a so-called Bravais lattice vector [12] [26]. Because of the periodicity of the crystal, the effective potential $V_{eff}(\vec{r})$ of Equation (4.3.6) satisfies the condition $V_{eff}(\vec{r}+\vec{R}) = V_{eff}(\vec{r})$.

Consequently, for this crystal, the electronic orbitals of Equation (4.3.6) can be labelled by the wavevector $\vec{k}$ (instead of the index "i") and satisfies Bloch's theorem However, for a periodic system recast Bloch's theorem [12],

$$\phi_k(\vec{r}) = \exp(\imath\vec{k}.\vec{r})u_k(\vec{r}). \tag{4.5.1}$$

where $u_k(\vec{r})$ is a periodic function with $u_k(\vec{r}) = u_k(\vec{r}+\vec{R})$ i.e u_k has the periodicity of the crystal and can, thus be expanded in a Fourier series as:

$$u_k(\vec{r}) = \sum_{\vec{G}} c_{\vec{k},\vec{G}} \exp(\imath\vec{G}.\vec{r}), \tag{4.5.2}$$

where $\vec{G}$ are the reciprocal lattice vectors satisfying $\frac{\vec{G}.\vec{R}}{2\pi}$ = integer and $c_{\vec{k},\vec{G}}$ are expansion coefficient to be determined by solving the K-S equation. The wave function of a periodic system, is thus,

$$\psi_k(\vec{r}) = \sum_{\vec{G}} c_{\vec{k},\vec{G}} \exp(\imath(\vec{G}+\vec{k}).\vec{r}). \tag{4.5.3}$$

This basis set has several advantages such as normalized, independent of ionic positions and can be used for Fast Fourier Transformation (FFT). Moreover, it can be simply represented on a computer. In principle Equation (4.5.3) represents an infinite number of plane waves. But, in practice Fourier components $c_{\vec{k},\vec{G}}$ for large $|\vec{k}+\vec{G}|$ are small, thus, they can be neglected. Therefore, the expansion is truncated at a specific value of $|\vec{k}+\vec{G}|$ in a unit of energy according to the following inequality,

$$\frac{\hbar^2|\vec{k}+\vec{G}|^2}{2m} \leq E_{cut}, \tag{4.5.4}$$

where E_{cut} is a cut-off energy.

4.5.2 The Pseudo-Potential Approximation

Even with this plane wave basis function, solving the electronic problem remains a computational challenge due to the nuclear potential contaned in V_{eff}. Electrons experience a sum of Coulomb potential in solids each of which goes as $\frac{-Ze^2}{r}$ where, r is the distance between the electron and the nuclear of charge $+Ze$. A difficulty arises when representing wave-functions of core electrons, which are sharply peaked near nuclei and valance electrons wave-functions for which has lots of "wiggles" near the nuclei and, thus, need large cut-off energies E_{cut}. Solutions to this problem might be to ignore these wiggles and exclude core electrons from the solution. Here pseudo-potentials come into play. They replace nuclear potentials as shown in Figure 4.1. The choice of pseudo-potentials depends on the element, and there is a variety of pseudo-potentials developed over the years [28] e.g. ultrasoft and norm conserving pseudo-potentials. Different pseudo-potentials need to be developed for various correlation functionals and different elements. Once the electron problem is solved the ionic/nuclear part can now be studied in order to examine the behaviour of the ions. We use these pseudo-potentials in our calculations, to determine a broad range of the macroscopic quantities, for example, specific heat, sound velocity, infrared absorption and Raman absorption, the vibrational properties of the materials can be used. Since electrons set the changes in the energy of the material when the atoms are displaced, therefore

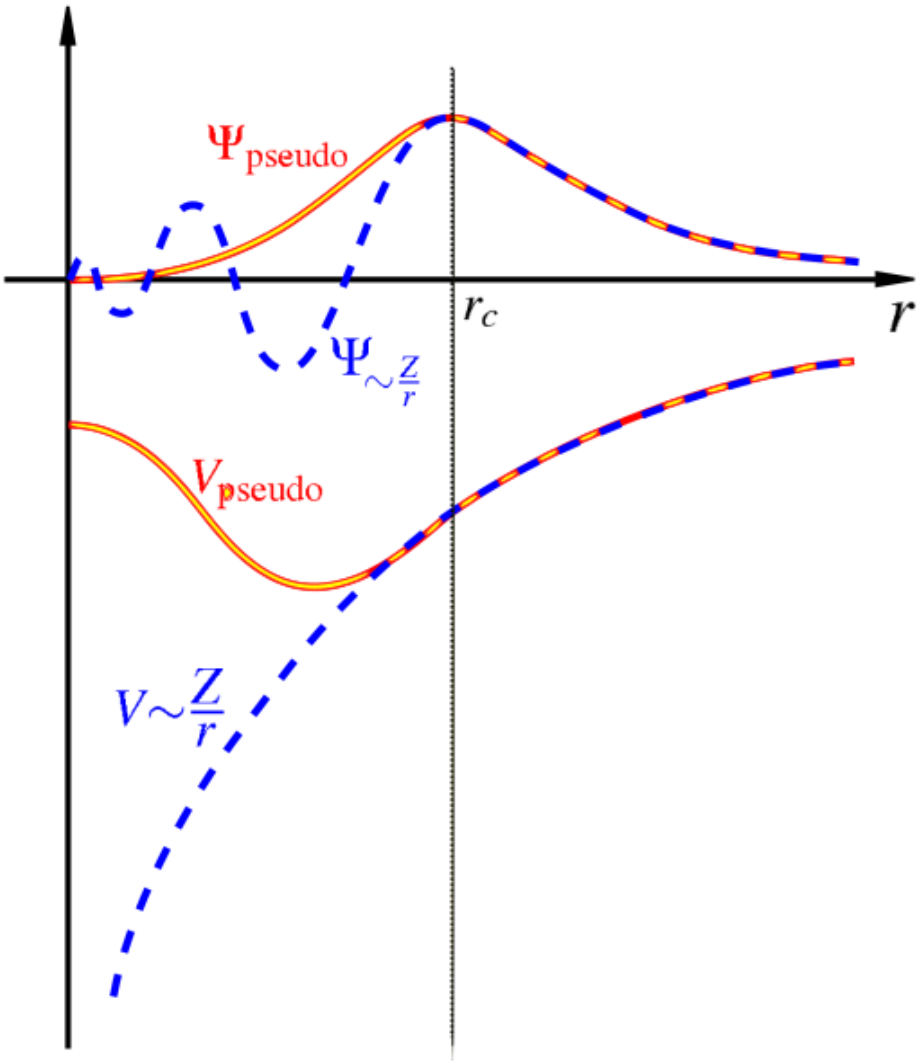

Figure 4.1: Schematic of the smoothing effect of the pseudo-wavefunction Ψ_{pseudo} and potential $\mathbf{V}_{pseudo}$ [27].

electronic structure contribute to the vibrational properties.

4.6 Calculations of Vibrational Frequencies

Previously, as mentioned in subsection 4.2.2 the BOA separated the electronic and nuclear degrees of freedom, thus assuming that the electronic energies do not depend on nuclear frequencies. once, since the nuclei are fixed the total energy $E(\vec{R}_I)$ will only depend on the positions of the nuclei $\vec{R}_I$ so the equation of motion of the nuclei can be written as follows:

$$M_I \frac{\partial^2 R_{I\alpha}}{\partial t^2} = F_{I\alpha} \equiv -\frac{\partial E(R_I)}{\partial R_{I\alpha}}, \tag{4.6.1}$$

where α denotes one of the spatial components (x, y, z). At equilibrium position $R^e_{I\alpha}$ all forces applied to an atom $F_I(R_0)$ must be zero. The harmonic approximation can be is used to obtain the frequencies ω of collective motion via from the atomic displacements $u_{I\alpha}(t)$:

$$u_{I\alpha}(t) = R_{I\alpha}(t) - R^e_{I\alpha} = \frac{\tilde{u}_I}{\sqrt{M_I}} \exp(\imath\omega t). \tag{4.6.2}$$

In the last term of Equation (4.6.2) above, we need some frequency ω for all ions since we are interested in collective motion of the ions. Using Expression (4.6.2) in Equation (4.6.1) gives:

$$-\omega^2 \tilde{u}_{I\alpha} = -\sum_{J\beta} C_{I\alpha,J\beta} \frac{\tilde{u}_{J\beta}}{\sqrt{M_I M_J}}, \tag{4.6.3}$$

where $C_{I\alpha,J\beta}$ are the force constants defined as,

$$C_{I\alpha,J\beta} = \frac{\partial^2 E(R)}{\partial R_{I\alpha} \partial R_{J\beta}}. \tag{4.6.4}$$

Equation (4.6.3) is an eigenvalue equation with ω^2 as the eigenvalues and $\zeta_{J\beta}$ are the eigenvectors. For non-trivial solutions, as usual, must have:

$$\det |\underline{D}(\vec{q}) - \omega^2 \underline{\mathbb{I}}_{3n\times 3n}| = 0, \tag{4.6.5}$$

where $\underline{D}(\vec{q}) = \sum_{J\beta} \frac{\tilde{u}_{J\beta}}{\sqrt{M_I M_J}} C_{I\alpha,J\beta}$ is the dynamical matrix and $\underline{\mathbb{I}}_{3n\times 3n}$ is the identity matrix. Solving Equation (4.6.5) after introducing $\tilde{u}_{J\beta} \sim \sum_{\vec{q}} \exp^{\imath \vec{q}.\vec{R}} f_{\vec{q}}$ gives $\omega^2 = \omega^2(\vec{q})$ i.e. the frequencies as functions of the wave-vector $\vec{q}$. The vibrational modes are determined by diagonalizing the dynamical matrix $\underline{D}(\vec{q})$, $\underline{D}(\vec{q})\mathbf{e}_\lambda = \omega^2_\lambda \mathbf{e}_\lambda$

In this work, we are interested in the lowest non-zero value of $\omega(\vec{q} = 0)$ calculated

for the diamond solid under different pressures. We will refer to these simply as the frequency, ω. This is the optical frequency of zero wave-vector $\vec{q} = 0$. This frequency can be obtained by two different methods:

4.6.1 Frozen Phonon Method

When frequencies are obtained from the calculation of the total energy and forces as a function of the positions of the atoms the method is called **Frozen Phonon Method** [21]. Since the nuclei positions $\vec{R}_I$ are fixed (or "frozen") in the calculations.
We proceeded as follows:

- Introducing a small displacement of the atoms from their equilibrium positions
- Evaluating the dynamical matrix constructed from the force constant matrix in Equation (4.6.4) which represents the forces exerted due to the preformed displacements
- Calculating the vibrational frequencies using Equation (4.6.5)

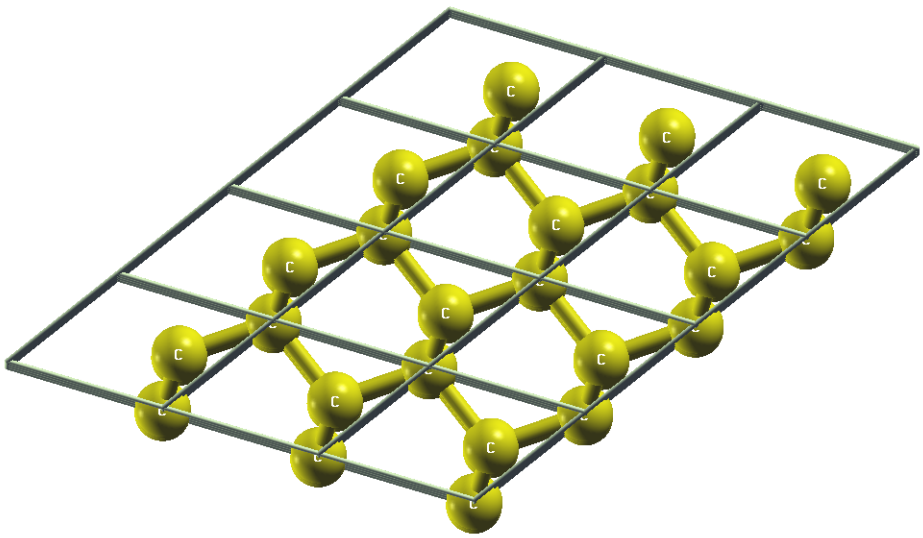

Figure 4.2: Illustration of the displacement of the atoms in the diamond unit cell [29].

The second approach for the calculations of ω is by the linear response method.

4.6.2 Linear Response

This method is based on calculating the force constant from linear perturbation theory in terms of the displacement from equilibrium positions [21].

From the comparison, we observed that using the frozen phonon method to calculate the vibrational frequency gives 1350 cm^{-1}, displaying the atoms by 0.002 in units of alat then calculating the force to determine the force constant using Hooke's law. However using linear response, we found the vibrational frequency 1336 cm^{-1} calculated at ambient pressure. The methods give results that agree within the overall approximations of the electronic structure calculations. From now on we will use the linear response method, due to its simplicity.

5 Results

In this chapter, we present our calculations and the obtained results. We started with convergence tests as shown below.

5.1 Convergence Tests

We have used the Quantum Espresso code [30] for first-principle calculations. To determine the vibrational frequencies, first, we have done convergence tests and obtained an optimal value for the lattice parameter as shown in Figure 5.1.

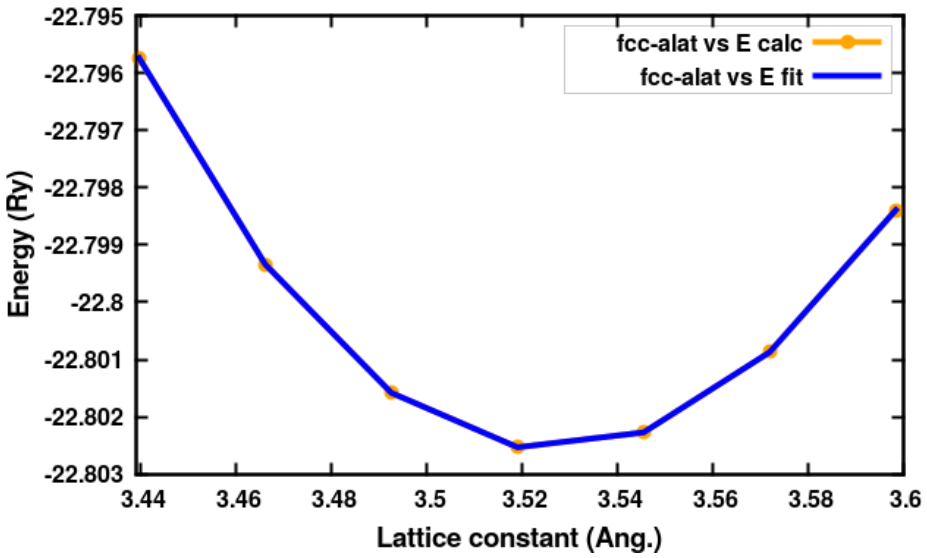

Figure 5.1: Plot of energy vs lattice constant, the data fitted to Murnaghan equation of state for a cubic diamond structure.

Quantity	Calculated	Experimental
Lattice parameter	3.52 Å	3.57 Å
Bulk modulus K_0	467 GPa	445±20 GPa
$K_0^{'}$	3.6	3.5 ± 0.5
ω_0	1334	1334 ± 1 cm^{-1}

Table 5.1.1: The properties of the cubic diamond structure were calculated and compared to the experimental data from [17], where ω_0 is the Raman line corresponds to the calculated value 1334 in the absence of stress (ambient conditions).

Additionally, we did optimization with respect to k-points, kinetic energy cut-off and

exchange-correlation functionals and pseudo-potentials.

The optimal value of the Brillouin zone integration was determined to be **8x8x8** of uniform grid points. The plane-wave basis set for the electronic wave functions has an optimal value at a kinetic energy cut-off of **130 Ry**.

The data from self-consistent calculations using the norm-conserving LDA pseudo-potential was fitted to the Murnaghan equation of state [31]. We obtained the equilibrium lattice constant to be **6.6639 a.u**. for fcc diamond structure which gave the minimum energy of the system as shown in Figure 5.1.

According to calculations conducted by Mutisye et al [32], they found that norm-conserving pseudo-potential and the LDA exchange-correlation functional (C.pz-vbc.UPF) agrees well with the fit of the experimental data by Dubrovinskaia et al [33] using the Expression (5.1.1) below,

$$\omega(P) = 1334.423069 + 2.259 \times P - 0.00146152 \times P^2, \tag{5.1.1}$$

where P is in gigapascals and ω is in cm^{-1}. Our calculations agree with their results as shown in Figure 5.2. The body-centred tetragonal (bct) unit cell of diamond shown in

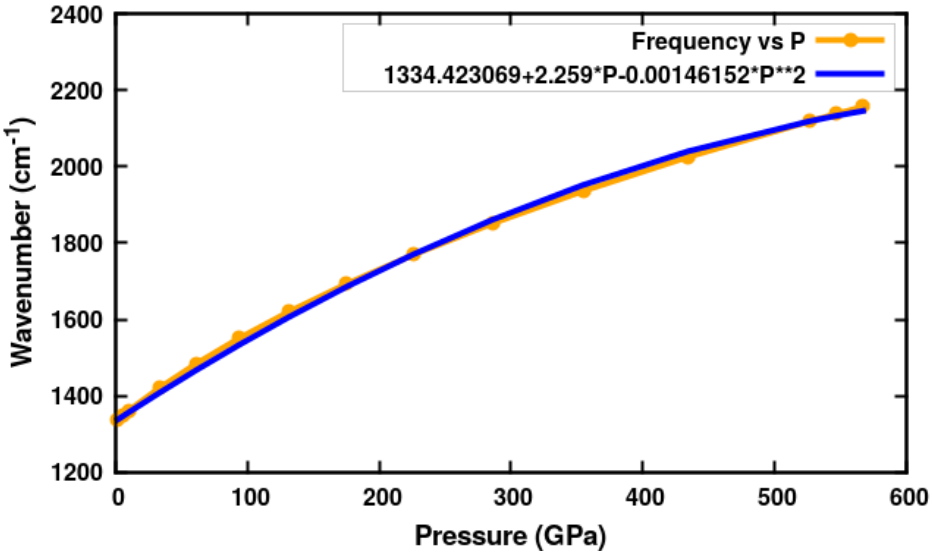

Figure 5.2: Shows the Raman frequency of the LTO optical phonon of diamond vs pressure in comparison to data using the norm conserving LDA pseudo-potential (C.pz-vbc.UPF).

the Figure 5.4 was used to calculate vibrational frequencies in the case of strain along the crystal direction [001] of the diamond to enable variation of c/a ratio.

Xcrysden [34] [29] was used to visualize the cubic diamond structure fcc as well as bct diamond structure, as shown in Figures 5.3 and 5.4, respectively.

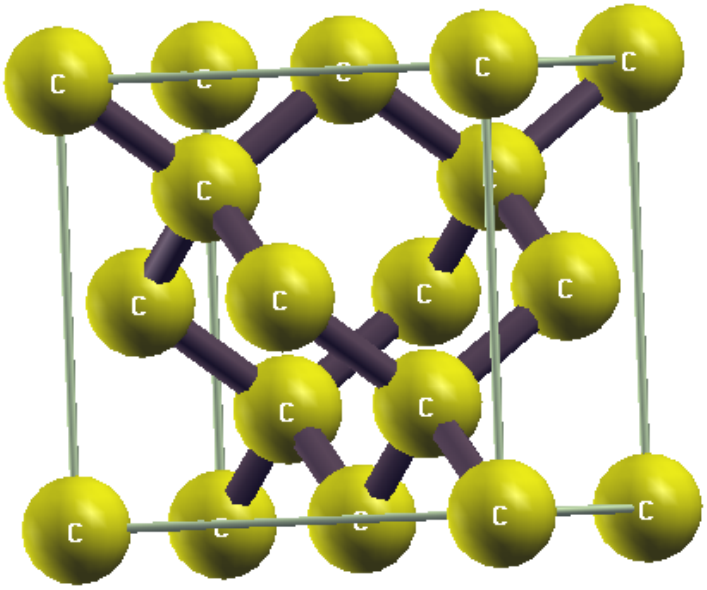

Figure 5.3: Diamond bct structure as visualized using Xcrysden [29].

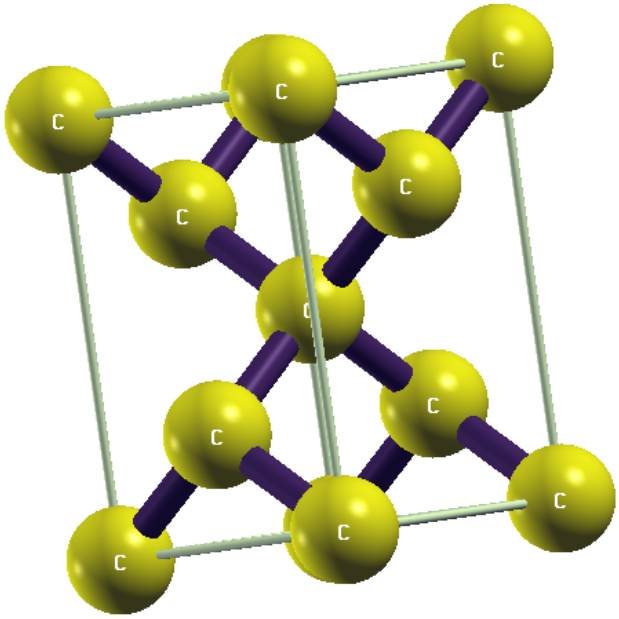

Figure 5.4: Diamond fcc structure as visualized using Xcrysden [29].

Next, we present our vibrational frequencies calculations, was done under:

1. Hydrostatic Compression
2. Non-Hydrostatic Compression

5.2 Vibrational Frequencies of Diamond under Hydrostatic Compression

As a result of the cubic symmetry of the diamond crystal structure the first-order Stokes-Raman spectrum of diamond is triply degenerated. Its optical phonons correspond to a single peak for wave-number of $\vec{q} \approx 0$ at ambient pressure. The Raman peak experiences a shift upon applying hydrostatic compression. We observed a monotonic dependence of the Raman peak of diamond on pressure, which is also in agreement with observations by Syassen and Hanflan [18].

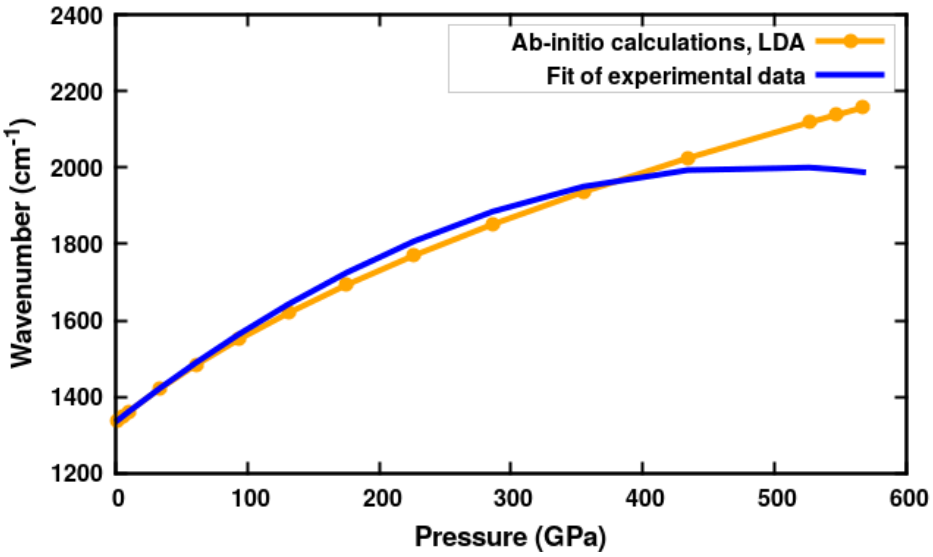

Figure 5.5: Shows the Raman frequency of the optical phonons of diamond vs pressure. shows that our ab-initio calculations are in a good agreement with the fit of experimental data by Dubrovinskaia et. al. [33] up to 300 GPa beyond that the experimental data doesn't exist.

5.3 Non-Hydrostatic Compression in the [001] Crystal Direction

However, in a DAC, the pressure on diamond crystal is not hydrostatic. Thus, the calculations of the vibrational frequencies under non-hydrostatic compression are of a great importance for us to an in-depth understanding of the stress state of the diamond culet face under millions of times of atmospheric pressure. Upon applying uniaxial stress along the crystal direction [001] corresponds to z-axis in our case. The corresponding stress tensor has the form:

$$\sigma = \begin{pmatrix} \sigma_r & 0 & 0 \\ 0 & \sigma_r & 0 \\ 0 & 0 & \sigma_z \end{pmatrix}, \tag{5.3.1}$$

with $\sigma_x = \sigma_y = \sigma_r \neq \sigma_z$. The average value of the pressure is

$$P_{\mathbf{average}} = \frac{(\sigma_z + 2\sigma_r)}{3}, \tag{5.3.2}$$

and the shear stress is given by

$$\tau = \sigma_z - \sigma_r. \tag{5.3.3}$$

The triply degenerate Raman band splits into a singlet and a doublet. In general under non-hydrostatic compression the triply degenerate Raman band splits depending on the axis of the applied stress. Thus, the split is described by the following equations:

$$\begin{aligned} F//[001] \qquad \omega_D &= \omega_H + \frac{2}{3}\Delta\omega_{[001]}, \\ \omega_S &= \omega_H - \frac{1}{3}\Delta\omega_{[001]}, \end{aligned} \tag{5.3.4}$$

where ω_S and ω_D are the singlet and doublet respectively, $F//[001]$ represents the uniaxial stress F which is parallel to the [001] crystal direction. While ω_H represents the shift in frequency due to a hydrostatic compression and $\Delta\omega_{[001]} = \omega_{S[001]} - \omega_{D[001]}$ is the splitting due to shear stress. For small shear stress Syassen and Hanfland [18] showed that $\delta\omega_{[001]} > 0$ and therefore, $\omega_D > \omega_S$. In experiments, experimentalists can only detect the singlet for the loading along [001] crystal direction due to symmetry constraints.

Notice, that the pressure on the sample is assumed to be σ_z. The vibrational

frequencies were calculated in the range of 150 GPa to 500 GPa for twenty different constant volume deformations. Here, we only considered this range because at low pressure values good pressure calibrants exist, e.g. the ruby fluorescence method as mentioned previously.

Since we assume that $\sigma_z > \sigma_r$ in DAC, we chose deformations such that the component of the stress perpendicular to the axis of the applied pressure σ_r is smaller than the component of the stress parallel to the axis of the applied pressure σ_z. At

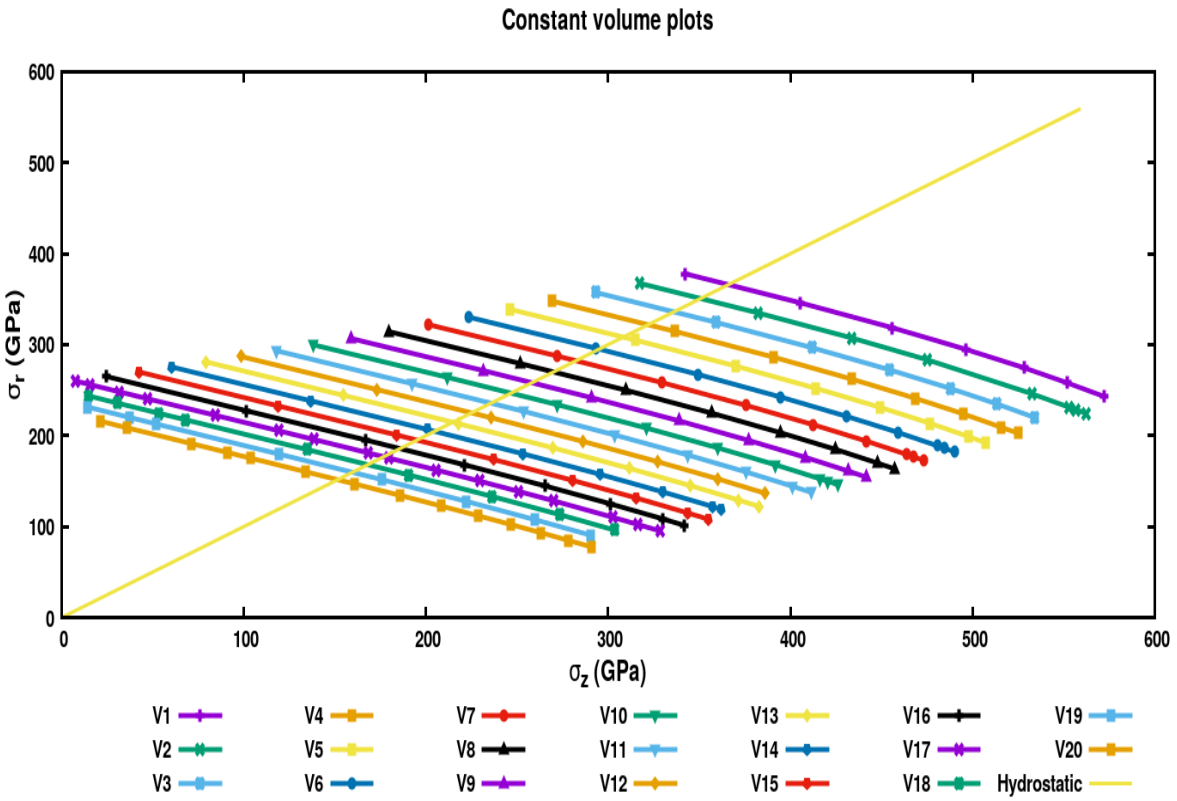

Figure 5.6: Variations of the axial and radial components of the stress. While V1 up to V20 represents the volumes which sets to be constant, are shown.

constant volumes the vibrational frequencies were obtained as shown in appendix A.1 for each of the constant volumes shown in Figure 5.6. Note, these calculations show a similar behaviour for all constant volumes, singlet and doublet are decreasing.
From our 20 constant volume calculations, we have obtained a large grid of σ_r and σ_z

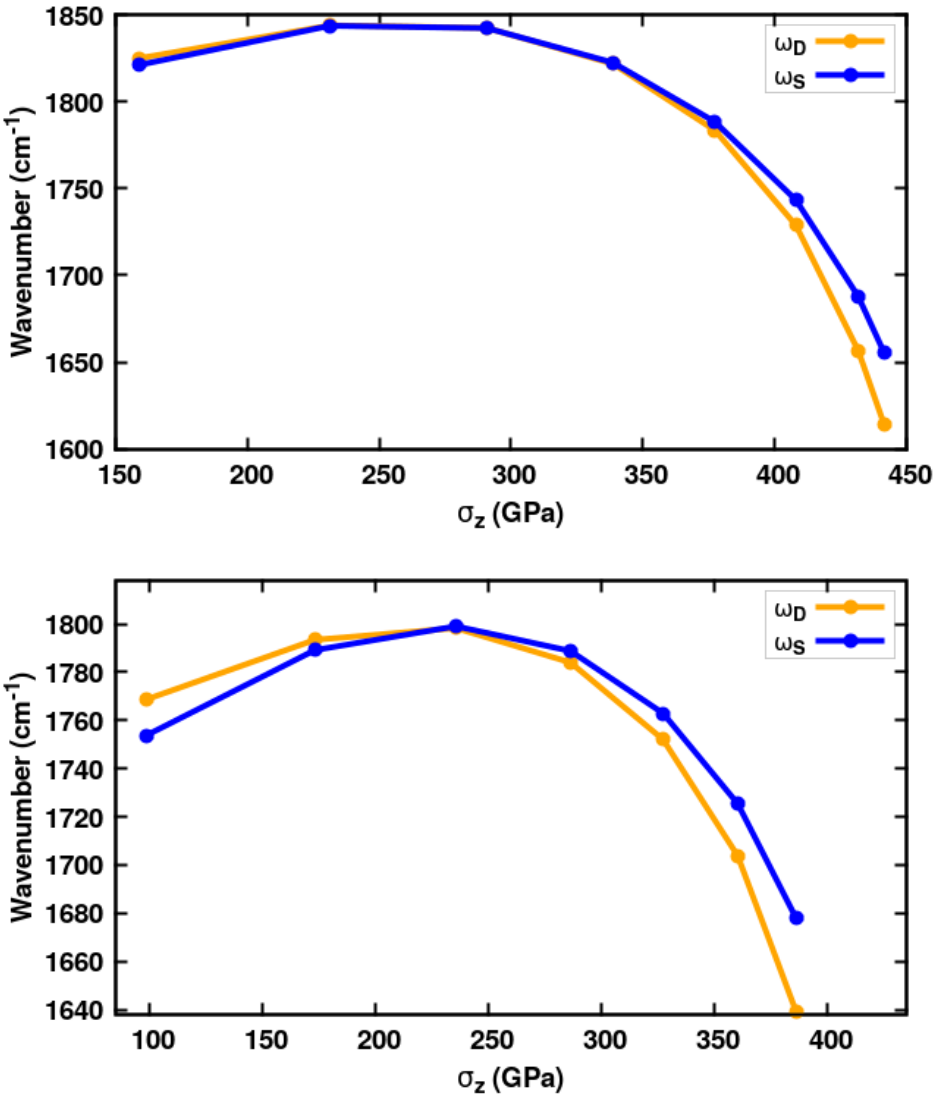

Figure 5.7: Shows the splitting of the singlet and the doublet under stress.

values which has been fitted to a polynomial of the following form:

$$\begin{aligned}\omega(\sigma_r,\sigma_z) &= \omega_H(P) - (a_0 + a_1(P-300) + a_2(P-300)^2)\tau \\ &- (b_0 + b_1(P-300) + b_2(P-300)^2)\tau^2 \\ &- (c_0 + c_1(P-300) + c_2(P-300)^2)\tau^3,\end{aligned} \tag{5.3.5}$$

where $\omega_H = \omega_0 + bP + cP^2$ is the Raman frequency calculated under hydrostatic conditions, $\omega_0 = 1334.423069$ cm^{-1} was obtained from the fit of the Murnaghan equation of state shown in table 5.1.1, P in GPa follows from Expression (5.3.2) and the shear stress τ from Expression (5.3.3).

Parameter	$\omega_{D[001]}$ fit	$\omega_{S[001]}$ fit
b	2.44587	2.44587
c	-0.002203695	-0.002203695
a_0	-0.0788613	-0.0167627
a_1	0.00113592	0.00156857
a_2	1.69068×10^{-5}	1.02681×10^{-6}
b_0	0.000370107	0.000595973
b_1	-2.37295×10^{-5}	-1.99886×10^{-5}
b_2	-1.06033×10^{-7}	-9.95841×10^{-8}
c_0	7.99371×10^{-6}	5.93023×10^{-6}
c_1	4.42136×10^{-8}	4.72882×10^{-8}
c_2	3.56219×10^{-11}	6.22401×10^{-11}

Table 5.3.1: Shows the obtained parameters which gave a good fit to the calculated data as shown in appendix A.2.

From the constant volume plots we were able to interpolate our data and obtain vibrational frequencies as shown in Figure 5.8. Therefore, using the function in Expression (5.3.5) we can predict the vibrational frequency for arbitrary values of σ_r and σ_z with an error of ± 30 cm^{-1}.

However, experimentalists can find the pressure using a measured value of the Raman frequency as well as the pressure in the sample σ_z and its corresponding σ_r value from Expression (5.3.5). This shows the importance of our calculations for experimentalists. Which will lead to an improvement in the diamond anvil design as

well as its geometry this can only be achieved by understanding the stress state of the diamond anvil culet face facing the sample. Upon applying the stress we can obtain information on how the sample is deformed.

Our calculations of the doublet ω_D and the singlet ω_S show that the doublet is not necessarily larger than the singlet. This is in contrast to small shear stress, where this is always the case. The figures of appendix A.1 illustrate this finding.

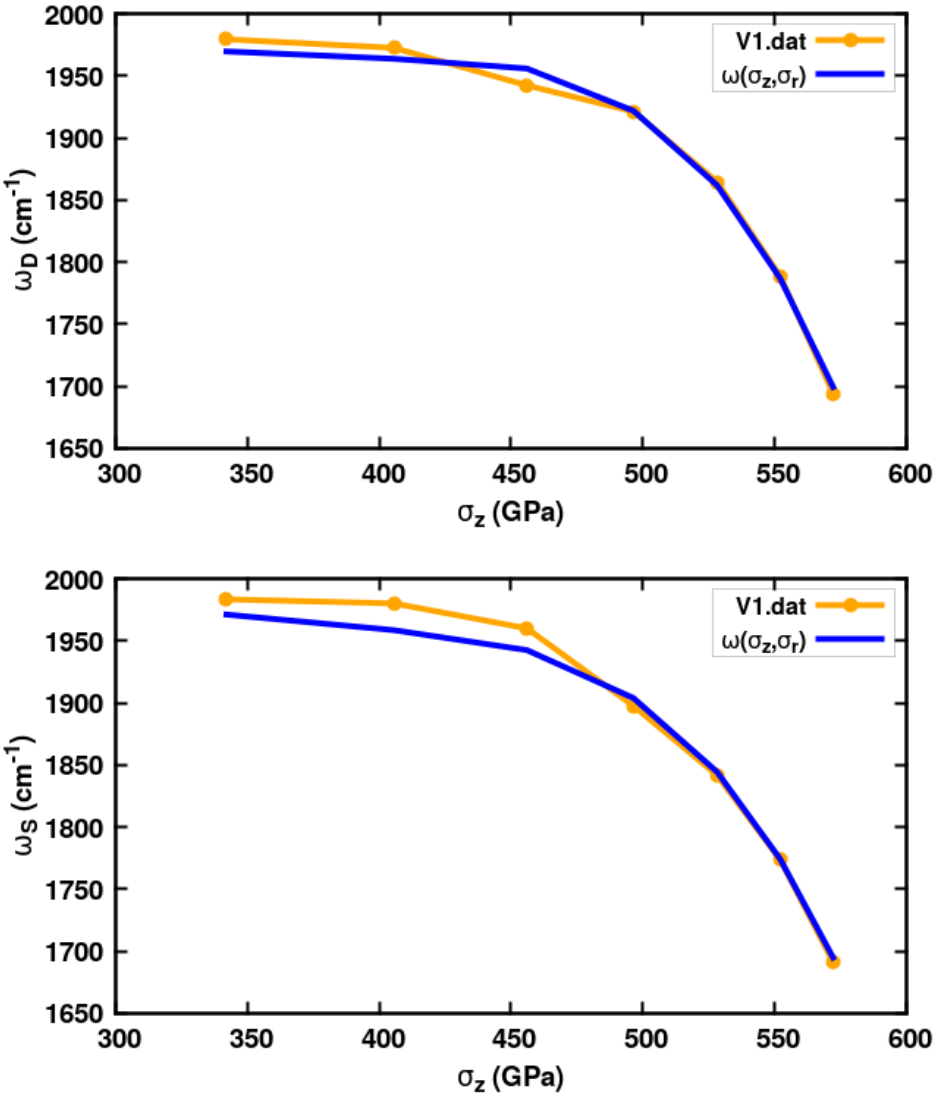

Figure 5.8: The blue line correspond to the fit of the Expression (5.3.5) and the orange line correspond to the constant volume (V1, as shown in Figure 5.6) obtained data.

In addition to Expression (5.3.5), we propose the following:

$$\begin{aligned}\omega(\sigma_r,\sigma_z) &= 1334.423069 + bP + cP^2 - (a_0 + a_1(P-300))\tau \\ &- (b_0 + b_1(P-300))\tau^2 - (c_0 + c_1(P-300))\tau^3,\end{aligned} \tag{5.3.6}$$

which provides as well a good fit to the calculated data. Thus, comparing the results

Parameter	$\omega_{D[001]}$ fit	$\omega_{S[001]}$ fit
b	2.433615	2.433615
c	-0.00210411	-0.00210411
a_0	-0.115405	-0.0510117
a_1	-0.00107958	0.000292495
b_0	0.00130992	0.00138632
b_1	-3.31409×10^{-7}	-1.7884×10^{-6}
c_0	5.23063×10^{-6}	3.61741×10^{-6}
c_1	1.0104×10^{-8}	1.07198×10^{-8}

Table 5.3.2: Shows the obtained parameters which gave a good fit to the calculated data. Corresponding figures are presented in appendix A.3.

obtained form the fit of Expression (5.3.5) with the fit of Expression (5.3.6), we find that Expression (5.3.5) gives a better fit, as shown in table 5.3.3. The quality of the fit can be known from the obtained values of the root mean square error (rms), as shown in the table below:

The function	$\omega_{D[001]}$ cm^{-1}	$\omega_{S[001]}$ cm^{-1}
rms of the fit of Expression (5.3.5)	7.47497	9.80084
rms of the fit of Expression (5.3.6)	9.55257	11.3778

Table 5.3.3: Shows the root mean square error (rms) for ω_D and ω_S fit.

From our calculations the stress state σ_r, σ_z which corresponds to the Raman edge can be extracted by inverting Expression (5.3.5). Since, from experiments along the loading crystal axis [001], ω_S is known.

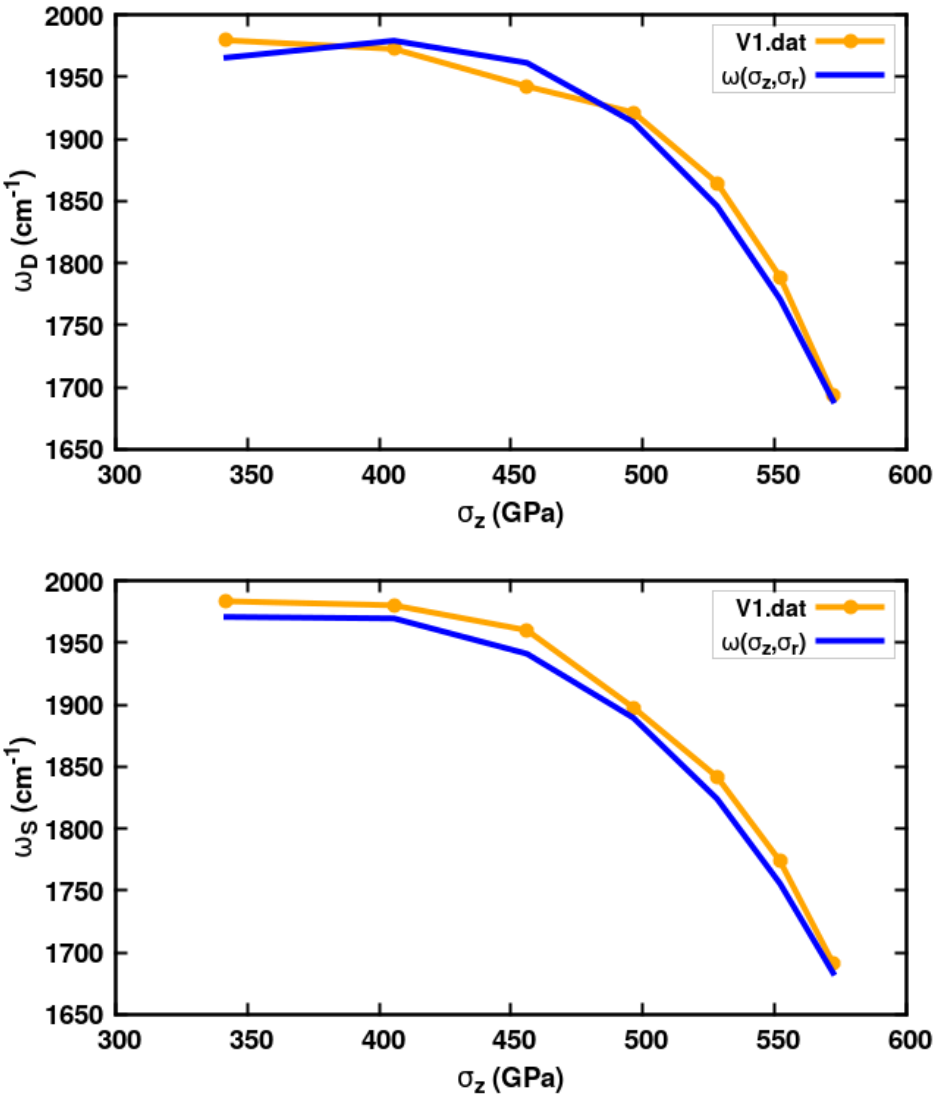

Figure 5.9: Interpolating data for constant volumes to Expression 5.3.6.

5.4 Shear Stress

In experiments σ_r is unknown and only ω_S is observed. We will assume that σ_r to be unknown in the following calculations and try to find it using the Expression (4.2.5). First, we calculate σ_z using the Expression below from Akahama et. al. [19]:

$$P = 3141 - 4.157\omega + 1.429 \times 10^{-3}\omega^2, \tag{5.4.1}$$

where P in GPa is equivalent to σ_z the pressure on the sample in our calculations and ω is the singlet ω_S. Akahama et al. [19] were able to estimate the pressure in the sample within the 2% error of the pressure value. We took ω_S in the range of [1710,1910] cm^{-1} and found the corresponding values of σ_z using the above expression. Then, known ω_S and the corresponding σ_z, we were able to compute σ_r by inverting the Expression in (5.3.5) and find the roots. The bisection method was used to calculate the roots which implies finding σ_r. Figure 5.10 shows the shear stress as a function of σ_z which diverges with increasing σ_z.

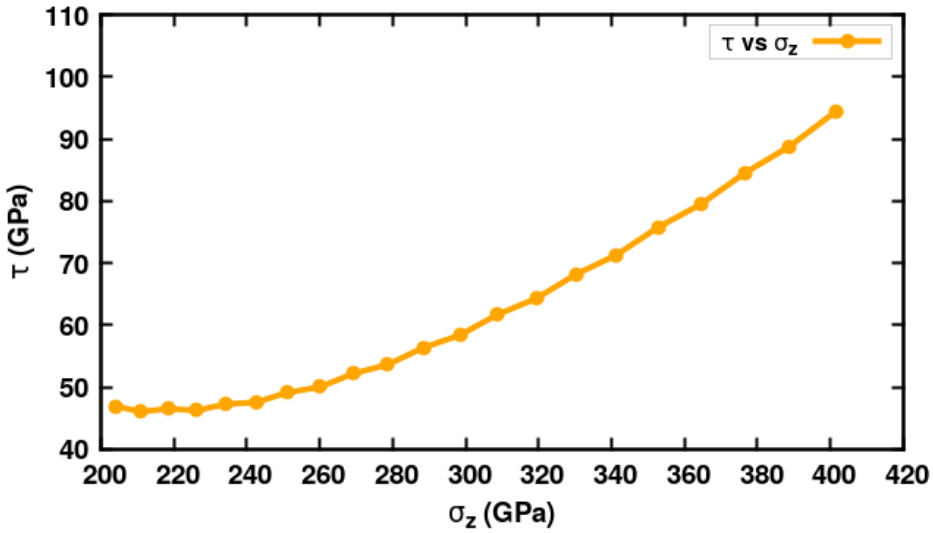

Figure 5.10: Shows the shear stress as a function of σ_z, calculated for vibrational frequencies provided by Akahama et. al. [19].

The table below shows the results obtained:

ω_s (cm^{-1})	σ_z (GPa)	σ_r (GPa)	τ (GPa)
1710	203.91000	157	46.91000
1720	211.06890	165	46.06890
1730	218.51360	172	46.51360
1740	226.24410	180	46.24410
1750	234.26040	187	47.26040
1760	242.56250	195	47.56250
1770	251.15040	202	49.15040
1780	260.02410	210	50.02410
1790	269.18360	217	52.18360
1800	278.62890	225	53.62890
1810	288.36000	232	56.36000
1820	298.37690	240	58.37690
1830	308.67960	247	61.67960
1840	319.26810	255	64.26810
1850	330.14239	262	68.14240
1860	341.30250	270	71.30250
1870	352.74840	277	75.74840
1880	364.48010	285	79.48010
1890	376.49760	292	84.49760
1900	388.80090	300	88.80090
1910	401.39000	307	94.39000

Table 5.4.1: Shows the obtained values of σ_r as well as the calculated values of τ. We have used Expression (5.4.1) to find σ_z, then, used Expression (5.3.5) to determine σ_r as shown. While $\tau = \sigma_z - \sigma_r$.

The error in the obtained values of σ_r is about 10 GPa. In experiments, the shear stresses are not measured. In these calculations, we were able to provide the corresponding values of it. As shown in table 5.4, τ can be found, by determining σ_r using our proposed Expression in (5.3.5). That could be a step further towards understanding the stress state of the diamond anvil cell.

6 Discussion and Conclusion

In this thesis, we have calculated using the ab-initio approach the vibrational frequencies of diamond under non-hydrostatic compression along the loading axis [001]. We observed the splitting of the triply degenerate first-order Raman mode, which results from the non-zero shear stress, $\sigma_z - \sigma_r \neq 0$. We have varied the radial and axial stress components at different constant volumes. As a result we found a simple polynomial approximation for the dependence of ω_D and ω_S on σ_r and σ_z.

Since in typical experiments ω_S is measured and σ_z is extracted from the pressure applied to the sample. We used Expression (5.3.5) to find σ_r (which is unknown to experimentalists) from the values of ω_S and the calculated values of σ_z are shown in table 5.4, with an error of 10 GPa in σ_r values. Then, we calculated the shear stress τ, the obtained values range up to 100 GPa at pressure of 400 GPa. This value of τ is less than the maximal value of the shear stress $\tau_{\mathbf{max}} = 200$, where the diamond is mechanically stable against tetragonal shear instabilities, and that found by [13], beyond $\tau_{\mathbf{max}}$ diamond is unstable against tetragonal shear instabilities. We believe that this could be important to determine the stress state of diamond in typical DAC experiments.

In future work, we plan to follow the same procedure for a loading along the crystal axis [111] and compare the results with the calculations done in this work.

Our calculations could be of a great importance to experimentalists who can utilize them for developing a better design and geometry of the diamond anvil cell. This will increase the maximal possible pressure that can be realised in experiments.

A Appendices

A.1 Plots shows the splitting of singlet and doublet under stress

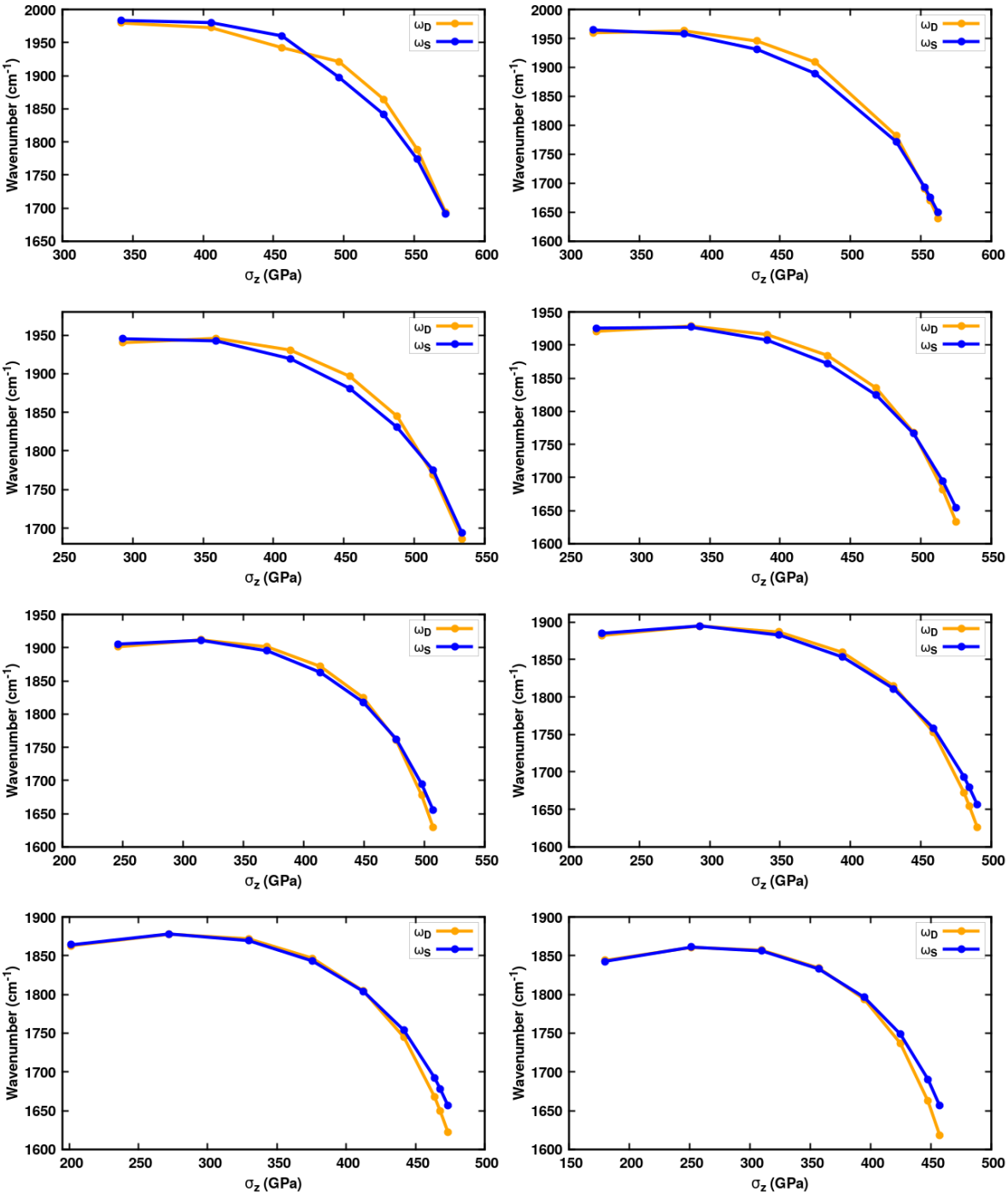

Figure A.1: Splitting of singlet and doublet under stress.

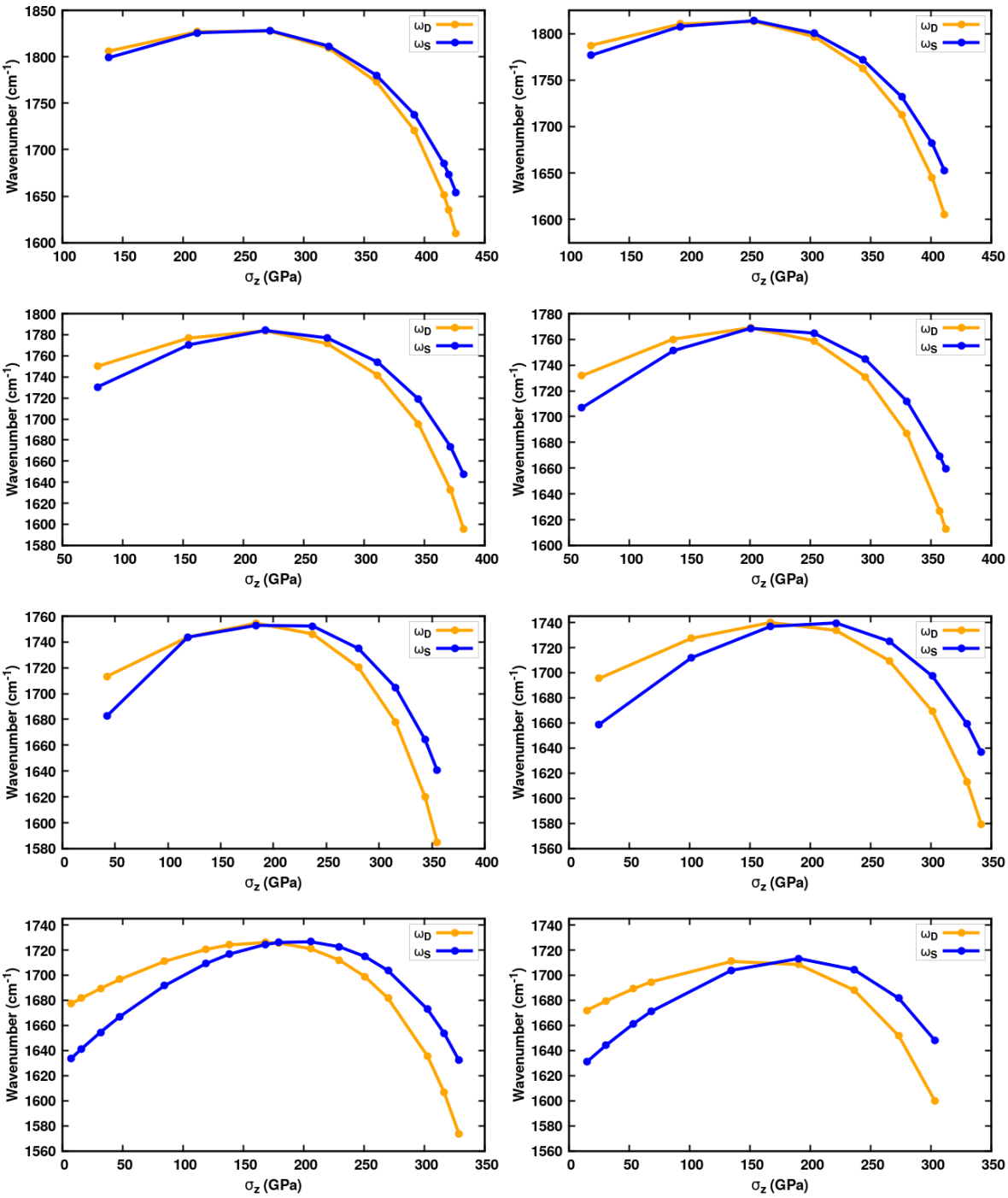

Figure A.2: Splitting of singlet and doublet under stress.

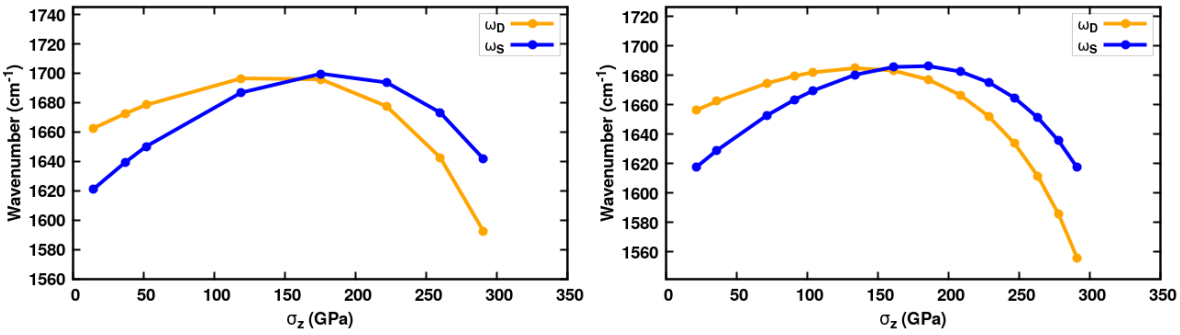

Figure A.3: Splitting of singlet and doublet under stress.

A.2 Fit of Expression (5.3.5)

In this section, we present the fit of Expression (5.3.5) of 20 constant volumes data.

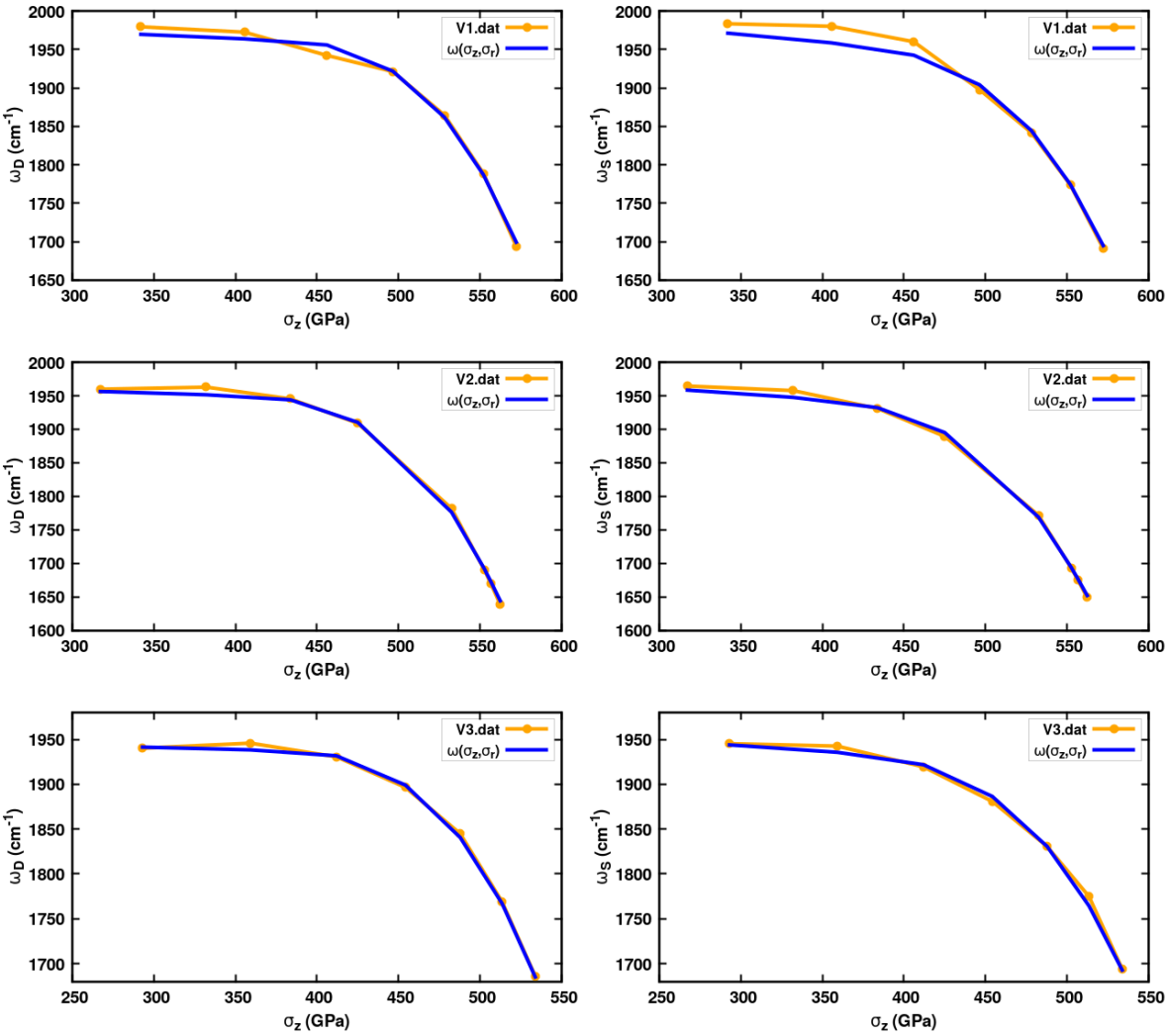

Figure A.4: Shows the fit of ω_D and ω_S of Expression (5.3.5).

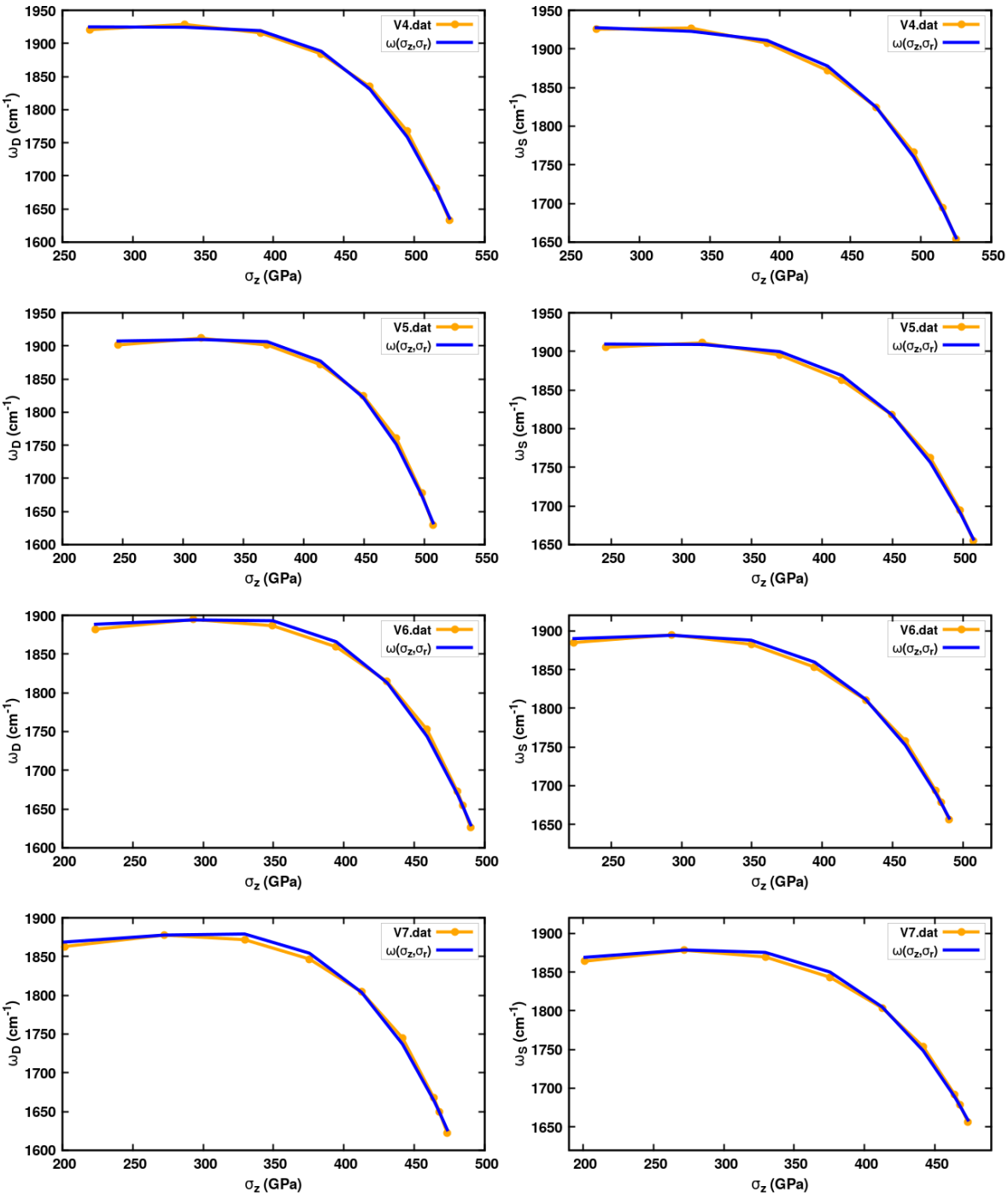

Figure A.5: Shows the fit of ω_D and ω_S of Expression (5.3.5).

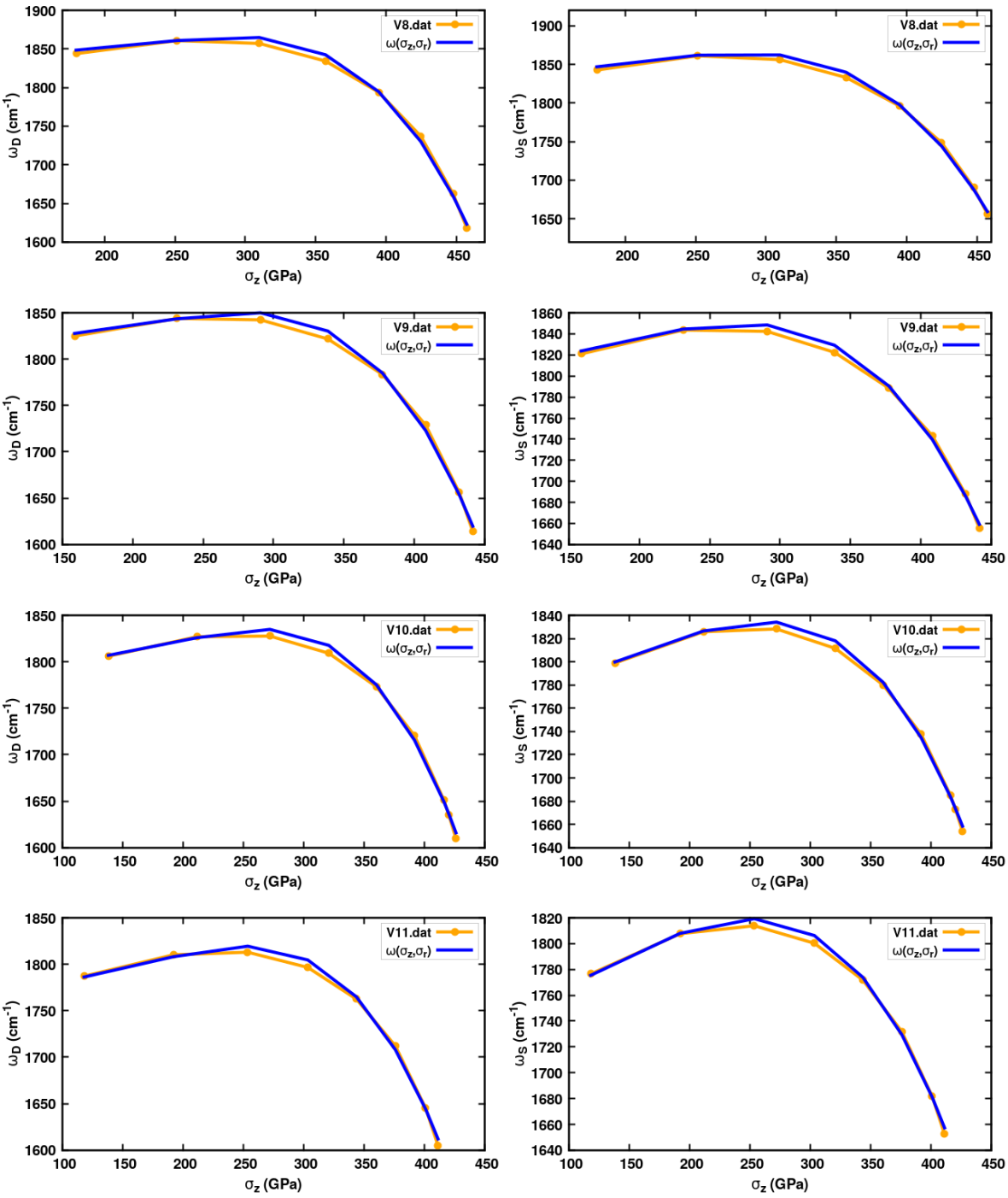

Figure A.6: Shows the fit of ω_D and ω_S of Expression (5.3.5).

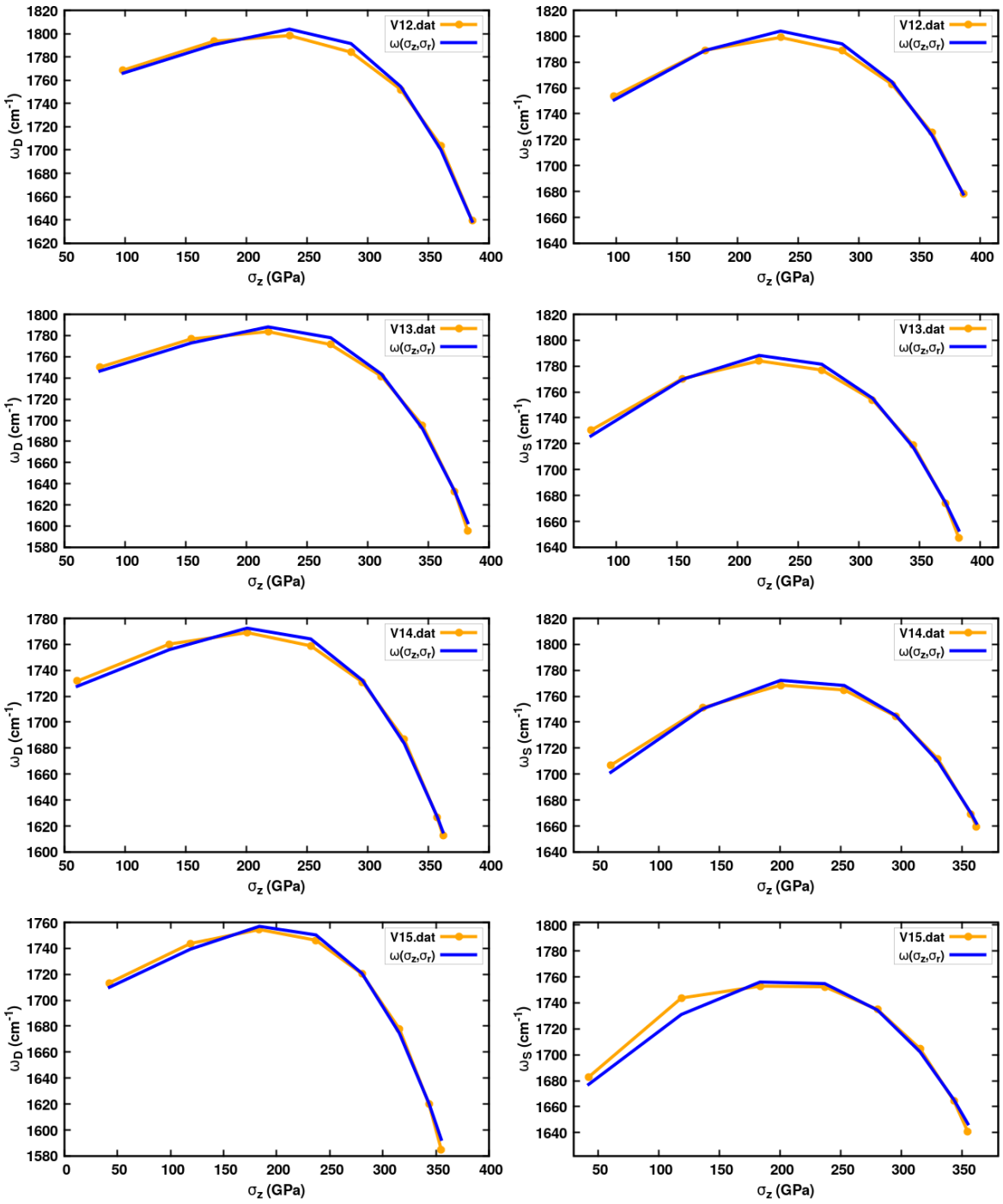

Figure A.7: Shows the fit of ω_D and ω_S of Expression (5.3.5).

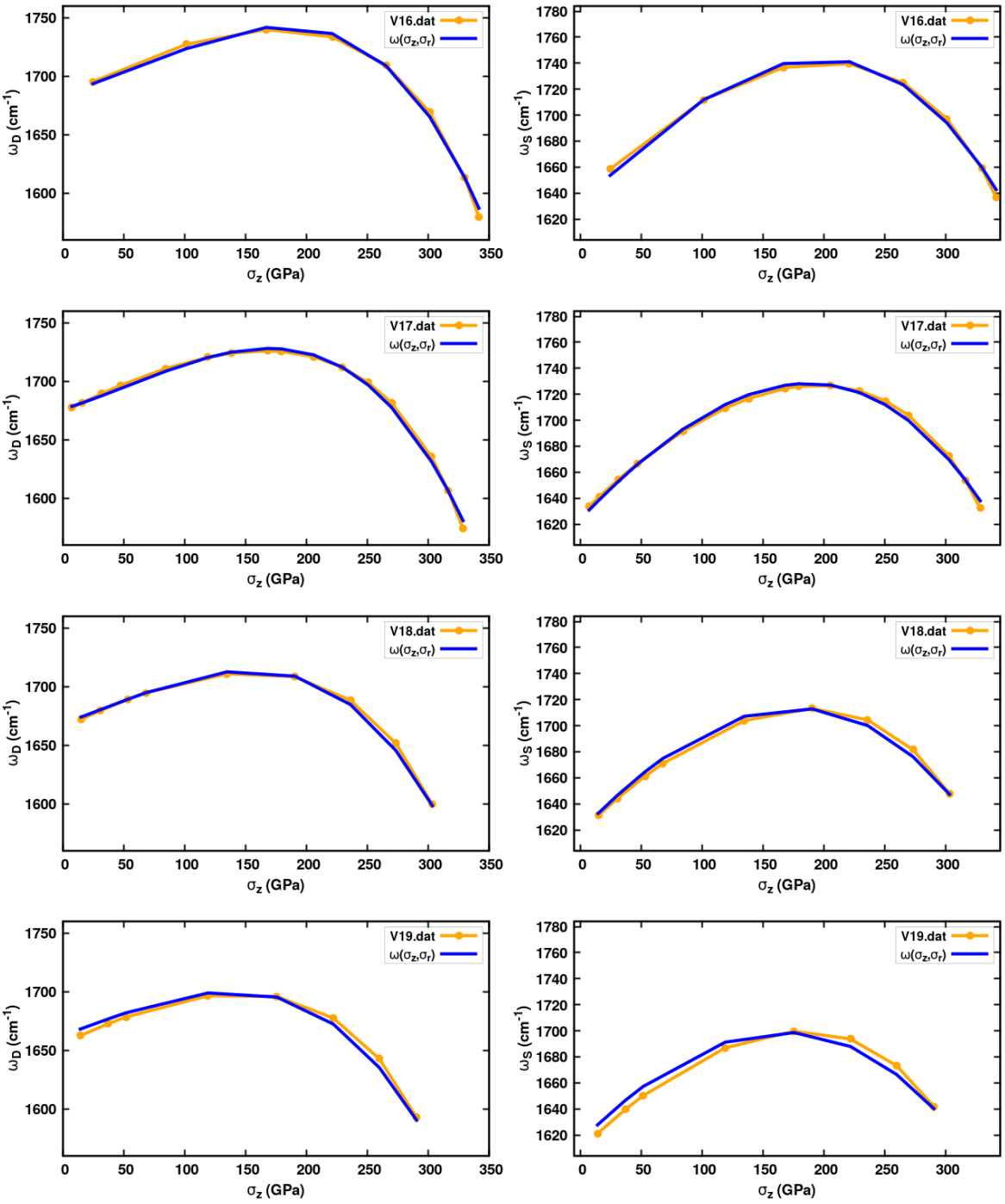

Figure A.8: Shows the fit of ω_D and ω_S of Expression (5.3.5).

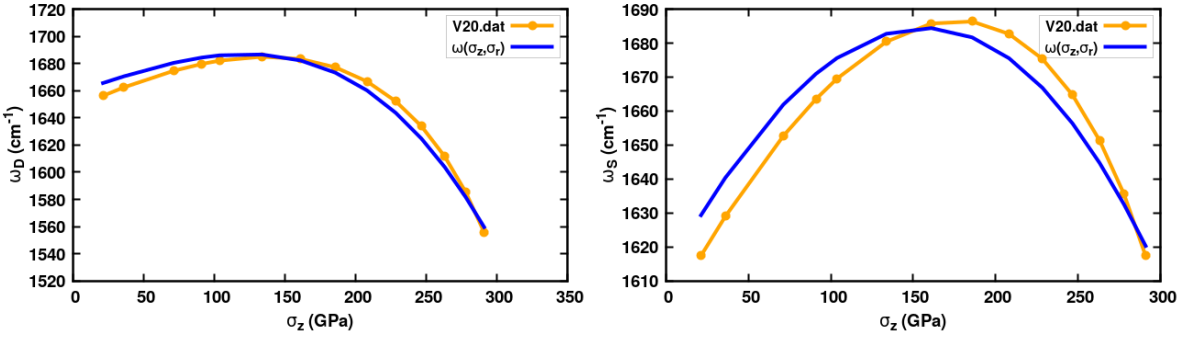

Figure A.9: Shows the fit of ω_D and ω_S of Expression (5.3.5).

A.3 Fit of Expression (5.3.6)

In this section, we present the fit of Expression (5.3.6) of 20 constant volumes data.

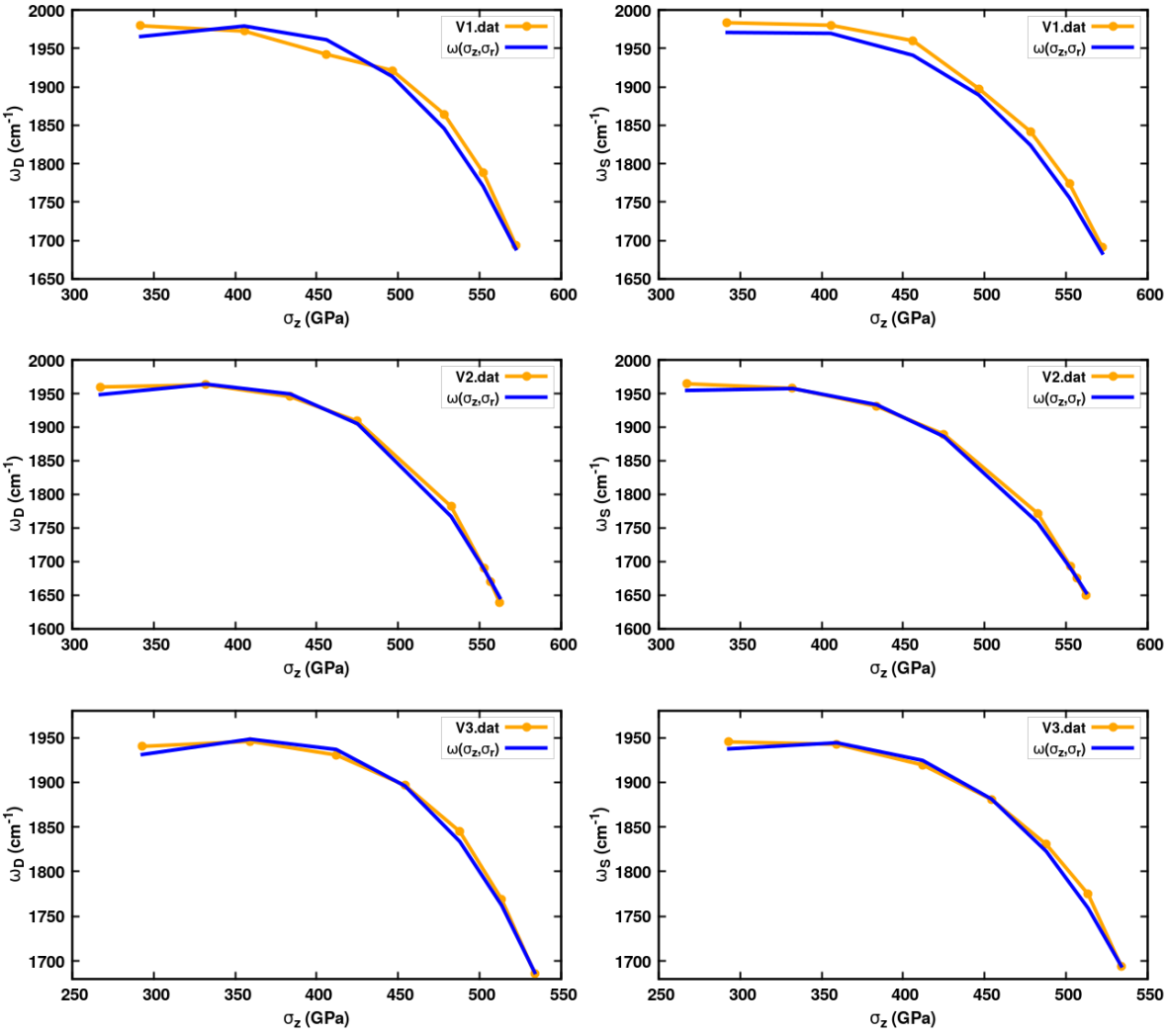

Figure A.10: Shows the fit of ω_D and ω_S of Expression (5.3.6).

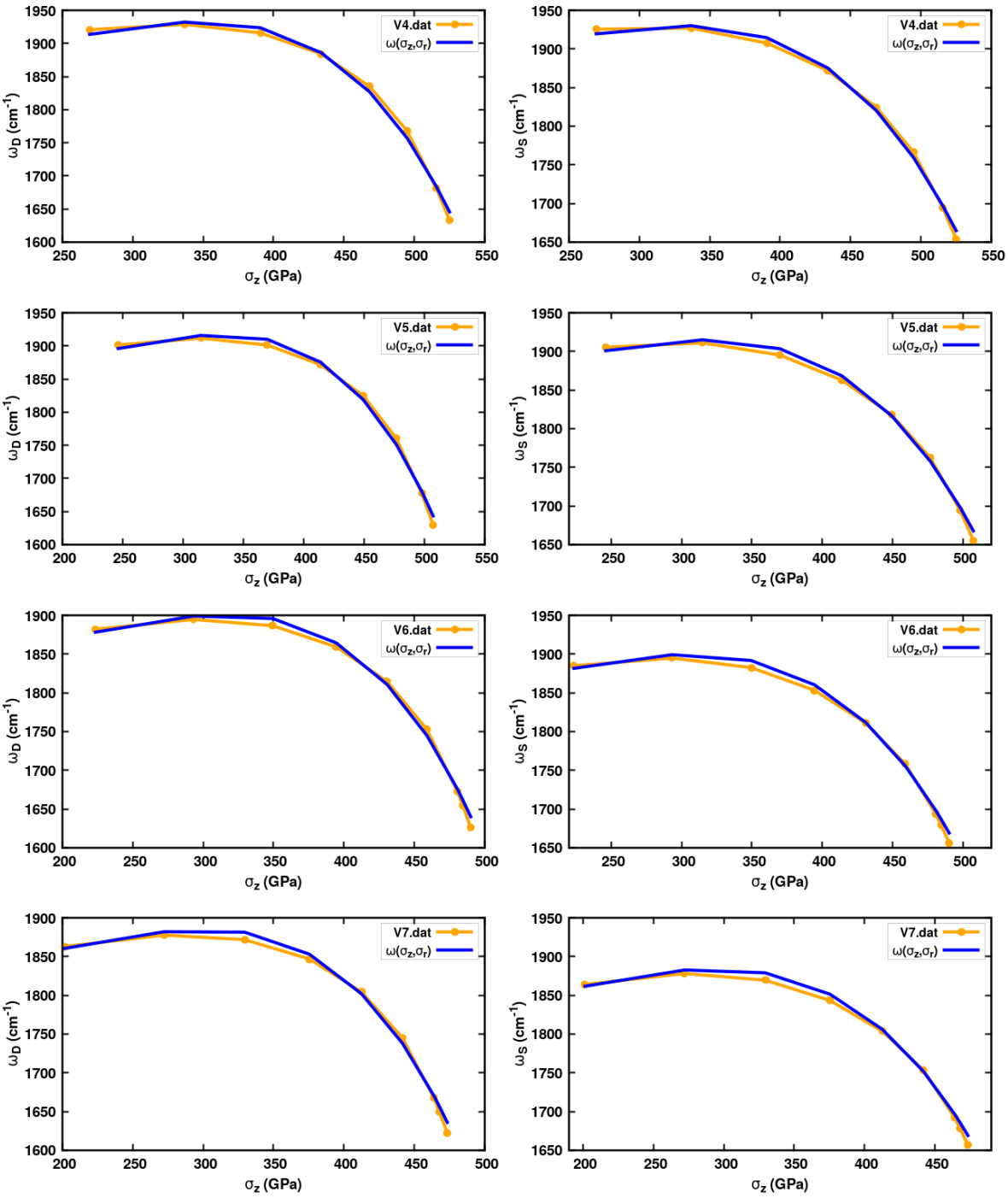

Figure A.11: Shows the fit of ω_D and ω_S of Expression (5.3.6).

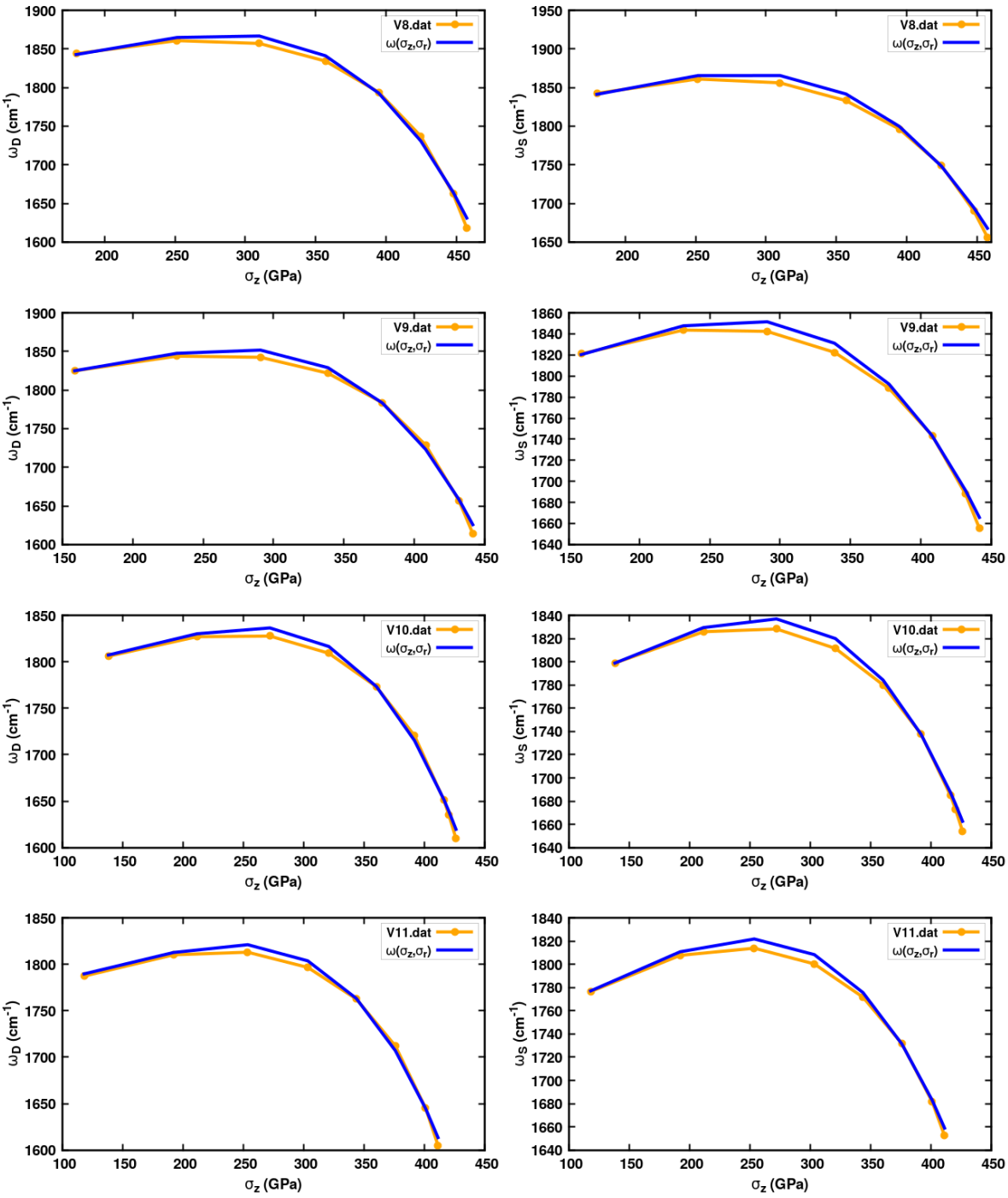

Figure A.12: Shows the fit of ω_D and ω_S of Expression (5.3.6).

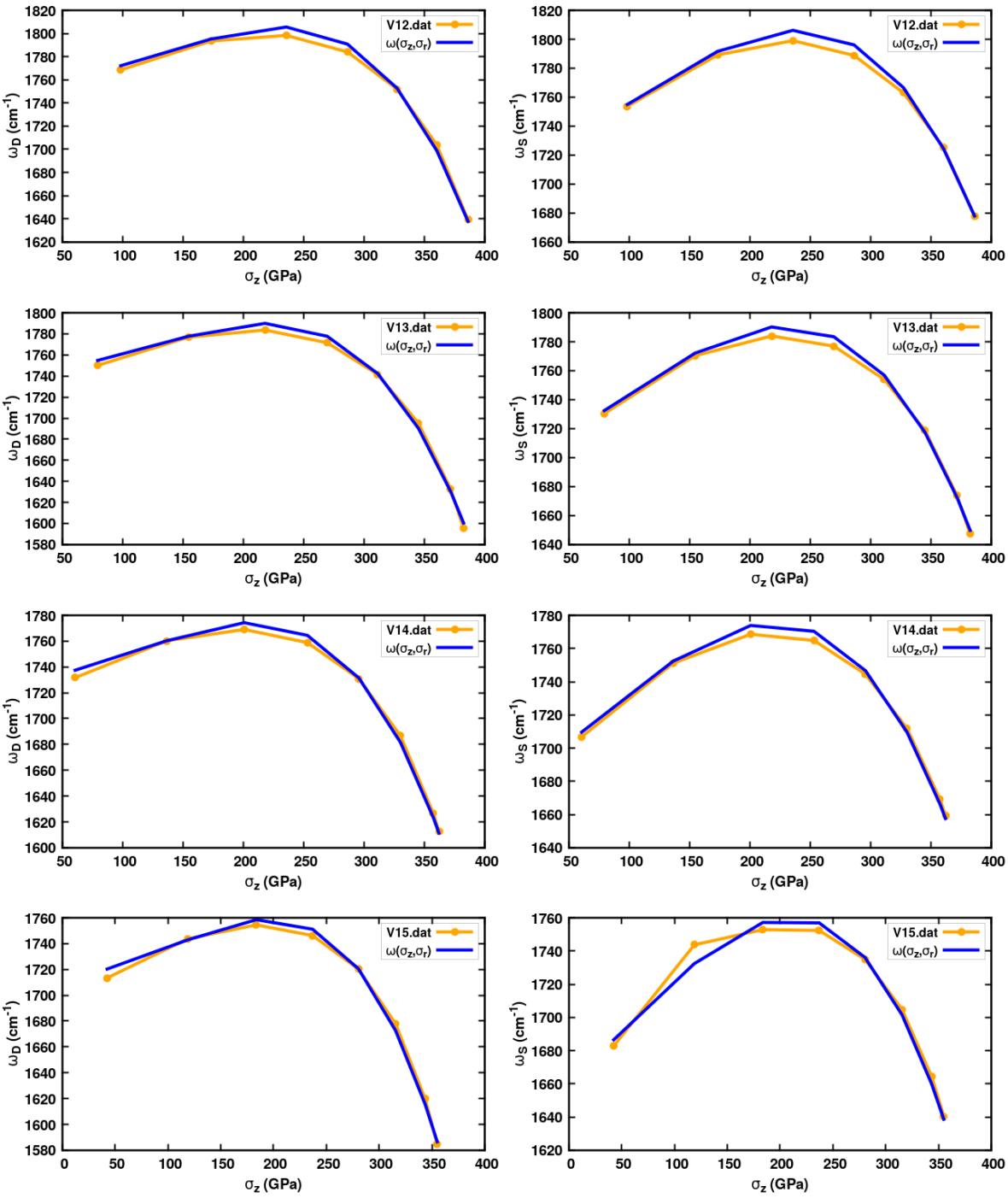

Figure A.13: Shows the fit of ω_D and ω_S of Expression (5.3.6).

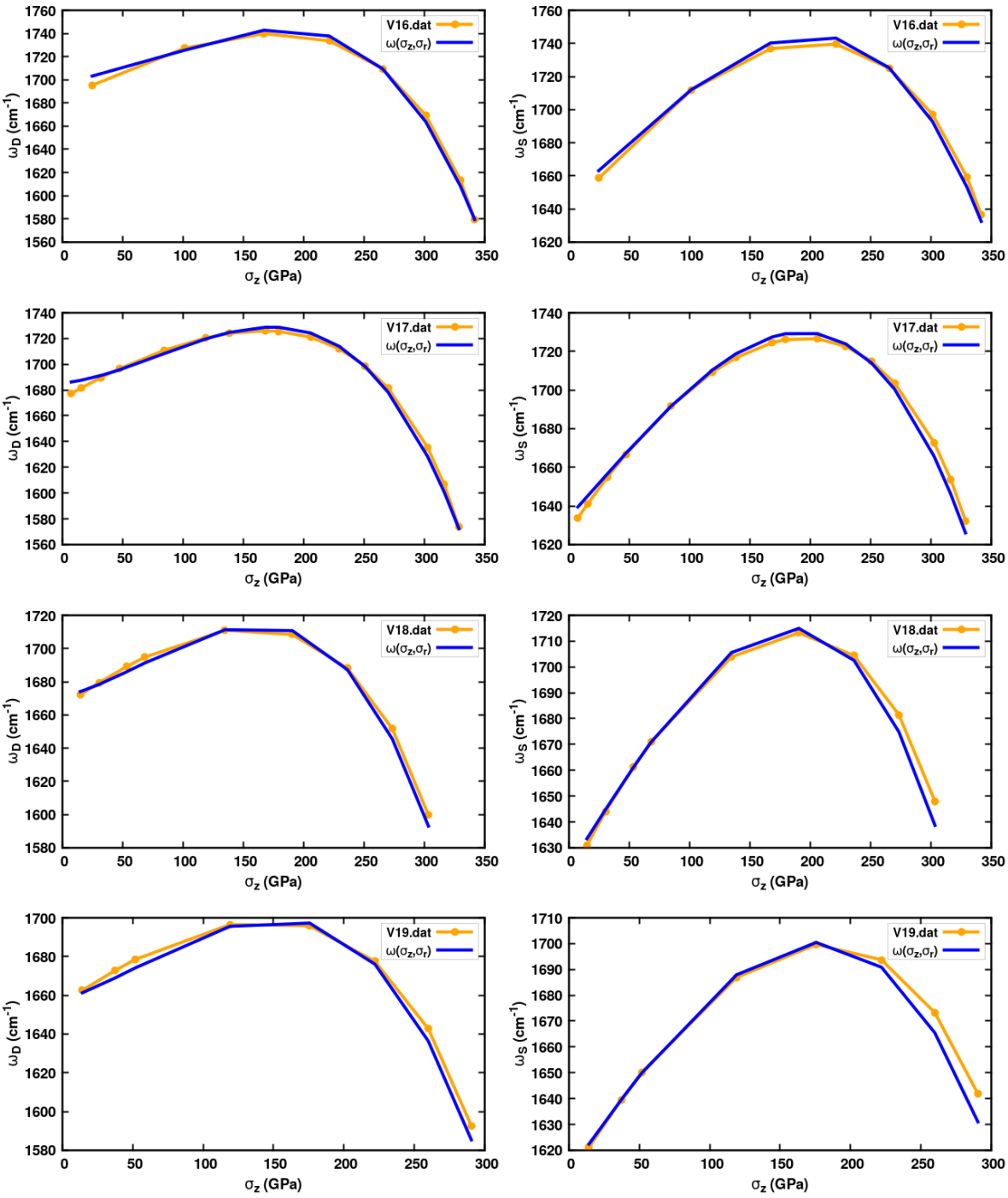

Figure A.14: Shows the fit of ω_D and ω_S of Expression (5.3.6).

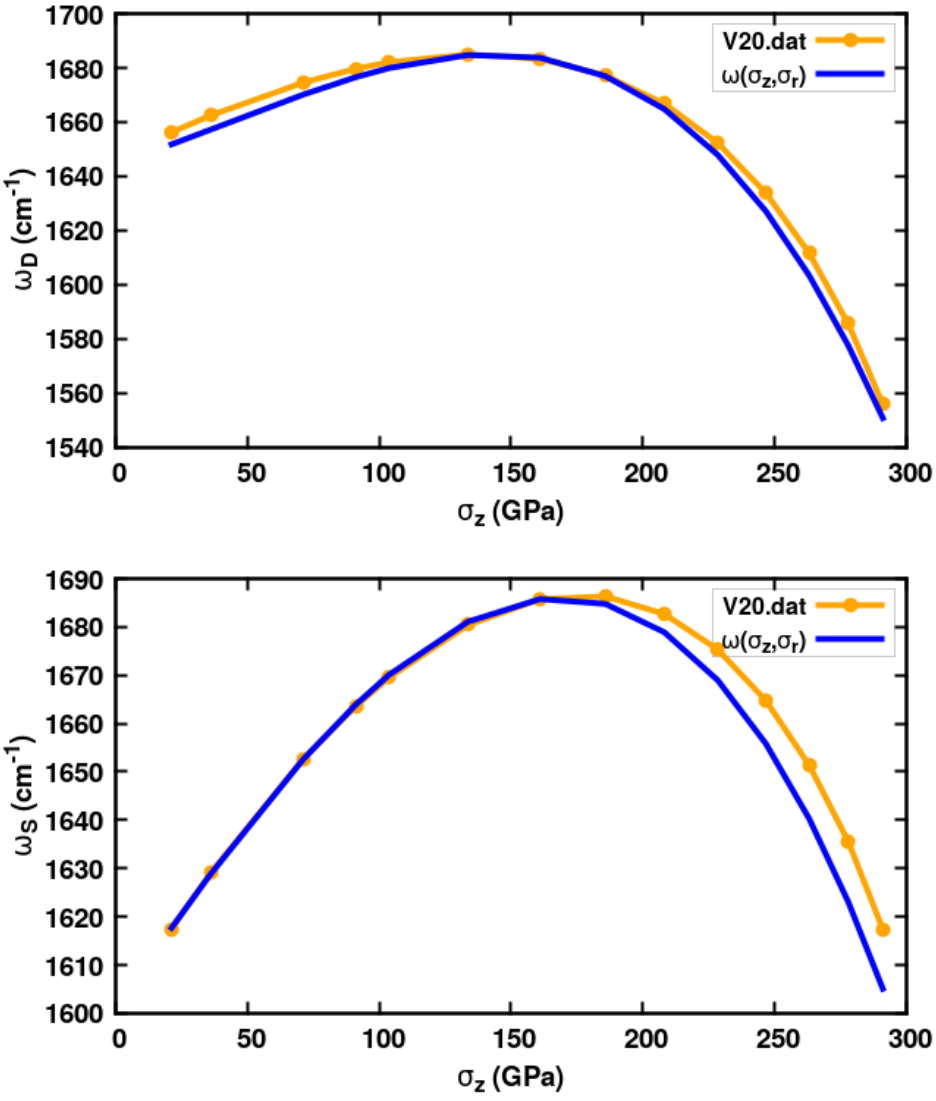

Figure A.15: Shows the fit of ω_D and ω_S of Expression (5.3.6).

A.4 Input files for body centered tetragonal diamond and cubic diamond

A.4.1 Input file for bct diamond

```
&control
 calculation = 'scf'
 restart_mode='from_scratch',
 prefix='D7',
 tstress = .true.
 tprnfor = .true.
 pseudo_dir = './',
 outdir='./'
 /
&system
 ibrav= 7,
 celldm(1)= 4.71,
 celldm(3) = 1.414213562,
 nat= 2,
 ntyp= 1,
 ecutwfc = 130,
 /
&electrons
 mixing_beta = 0.7
 conv_thr = 1.0d-8
 /
 &ions
 /
 &cell
  press=70.,
 /
 ATOMIC_SPECIES
 C 12.0107 C.pz-vbc.UPF
 ATOMIC_POSITIONS crystal
C 0.00 0.00 0.00
C 0.50 0.25 -0.25
 K_POINTS automatic
 8 8 8 0 0 0
```

A.4.2 Input file for fcc diamond

```
&CONTROL
   calculation = 'scf'
   restart_mode='from_scratch',
   prefix='D2',
   tstress = .true.
   tprnfor = .true.
   pseudo_dir = './',
   outdir='./'
/

&SYSTEM
   ibrav = 2
   celldm(1) = 6.6639
   nat = 2
   ntyp = 1
   nspin=2
   ecutwfc = 130
/

&ELECTRONS
   conv_thr = 1.0d-8
   mixing_beta = 0.7
/
&ions
 /
 &cell
  press=70.,
 /
ATOMIC_SPECIES
 C 12.011 C.pz-vbc.UPF
ATOMIC_POSITIONS crystal
 C 0.000 0.000 0.000
 C 0.250 0.250 0.250
K_POINTS automatic
 8 8 8 0 0 0
```

References

[1] Ranga P Dias and Isaac F Silvera. Observation of the wigner-huntington transition to metallic hydrogen. *Science*, 355(6326):715–718, 2017.

[2] Ravit Helled, Guglielmo Mazzola, and Ronald Redmer. Understanding dense hydrogen at planetary conditions. *Nature Reviews Physics*, 2020.

[3] Surinder M Sharma and Nandini Garg. Material studies at high pressure. In *Materials Under Extreme Conditions*, pages 1–47. Elsevier, 2017.

[4] Francesca PA Fabbiani and Colin R Pulham. High-pressure studies of pharmaceutical compounds and energetic materials. *Chemical Society Reviews*, 35(10):932–942, 2006.

[5] Natalia Dubrovinskaia, Leonid Dubrovinsky, Natalia A Solopova, Artem Abakumov, Stuart Turner, Michael Hanfland, Elena Bykova, Maxim Bykov, Clemens Prescher, Vitali B Prakapenka, et al. Terapascal static pressure generation with ultrahigh yield strength nanodiamond. *Science advances*, 2(7):e1600341, 2016.

[6] Shigehiko Tateno, Kei Hirose, Nagayoshi Sata, and Yasuo Ohishi. Solubility of feo in (mg, fe) sio3 perovskite and the post-perovskite phase transition. *Physics of the Earth and Planetary Interiors*, 160(3-4):319–325, 2007.

[7] D Yamazaki, E Ito, T Yoshino, N Tsujino, A Yoneda, X Guo, F Xu, Y Higo, and K Funakoshi. Over 1 mbar generation in the kawai-type multianvil apparatus and its application to compression of (mg0. 92fe0. 08) sio3 perovskite and stishovite. *Physics of the Earth and Planetary Interiors*, 228:262–267, 2014.

[8] Sergey V. Rashchenko. File:high-pressure experiments.png. High-pressure-experiments, 19 May 2017.

[9] Russell J Hemley. Percy w. bridgman's second century. *High Pressure Research*, 30(4):581–619, 2010.

[10] Young Ho Ko, Kwang Joo Kim, Chung Kyu Han, Cedomir Petrovic, Rongwei Hu, Hyun Hee Lee, and Yongjae Lee. Static compression of ϵ fesi. *Journal of the Korean Physical Society*, 56(3):832–835, 2010.

[11] Lawrence S Pan and Don R Kania. *Diamond: electronic properties and applications*. Springer Science & Business Media, 2013.

[12] Neil W Ashcroft, N David Mermin, et al. Solid state physics [by] neil w. ashcroft [and] n. david mermin., 1976.

[13] Ji-Jun Zhao, S Scandolo, J Kohanoff, GL Chiarotti, and E Tosatti. Elasticity and mechanical instabilities of diamond at megabar stresses: Implications for diamond-anvil-cell research. *Applied physics letters*, 75(4):487–488, 1999.

[14] Yuichi Akahama and Haruki Kawamura. Raman study on the stress state of [111] diamond anvils at multimegabar pressure. *Journal of applied physics*, 98(8):083523, 2005.

[15] Diamond structure. https://tex.stackexchange.com/questions/141363/draw-realistic-3d-crystal-structures-diamond, Jan 21 2020.

[16] HK Mao, PM Bell, JW t Shaner, and DJ Steinberg. Specific volume measurements of cu, mo, pd, and ag and calibration of the ruby r 1 fluorescence pressure gauge from 0.06 to 1 mbar. *Journal of applied physics*, 49(6):3276–3283, 1978.

[17] Yuichi Akahama and Haruki Kawamura. Pressure calibration of diamond anvil raman gauge to 310 gpa. *Journal of Applied Physics*, 100(4):043516, 2006.

[18] M Hanfland and K Syassen. A raman study of diamond anvils under stress. *Journal of applied physics*, 57(8):2752–2756, 1985.

[19] Yuichi Akahama and Haruki Kawamura. Pressure calibration of diamond anvil raman gauge to 410 gpa. *Journal of Physics: Conference Series*, 2010.

[20] Yuichi Akahama, Haruki Kawamura, and Singh A. K. High-pressure raman spectroscopy of diamond anvils to 250 gpa: Method for pressure determination in the multimegabar pressure range. *Journal of Applied Physics*, 96(7):3748–3751, 2004.

[21] Richard M Martin and Richard Milton Martin. *Electronic structure: basic theory and practical methods*. Cambridge university press, 2004.

[22] Attila Szabo and Neil S Ostlund. *Modern quantum chemistry: introduction to advanced electronic structure theory*. Courier Corporation, 2012.

[23] Andreas Görling. Density-functional theory beyond the hohenberg-kohn theorem. *Physical Review A*, 59(5):3359, 1999.

[24] Diola Bagayoko. Understanding density functional theory (dft) and completing it in practice. *AIP Advances*, 4(12):127104, 2014.

[25] John P Perdew and Kieron Burke. Comparison shopping for a gradient-corrected density functional. *International journal of quantum chemistry*, 57(3):309–319, 1996.

[26] Charles Kittel and Paul McEuen. *Introduction to solid state physics*, volume 8. Wiley New York, 1976.

[27] Wolfram Quester. File:sketch pseudopotentials.png. Sketch Pseudopotentials, 22 November 2006.

[28] Carlos Fiolhais, Fernando Nogueira, and Miguel AL Marques. *A primer in density functional theory*, volume 620. Springer Science & Business Media, 2003.

[29] Xcrysden. http://www.xcrysden.org/, October 2019.

[30] Quantum espresso. https://www.quantum-espresso.org, Version 2, June 1991.

[31] FD Murnaghan. The compressibility of media under extreme pressures. *Proceedings of the national academy of sciences of the United States of America*, 30(9):244, 1944.

[32] S. Mutisya. Vibrational frequencies of diamond under non hydrostatic compression: an ab-initio study. *Dissertetion thesis, ICTP Diploma in Condensed Matter Physics*, 2012.

[33] Natalia Dubrovinskaia, Leonid Dubrovinsky, Razvan Caracas, and Michael Hanfland. Diamond as a high pressure gauge up to 2.7 mbar. *Applied Physics Letters*, 97(25):251903, 2010.

[34] Anton Kokalj. Xcrysdena new program for displaying crystalline structures and electron densities. *Journal of Molecular Graphics and Modelling*, 17(3-4):176–179, 1999.